INVESTIGATING LOCAL GROWTH CONDITIONS IN THE FLAME SYNTHESIS OF METAL-OXIDE NANOSTRUCTURES

By

CASSANDRA D'ESPOSITO

A thesis submitted to the

Graduate School-New Brunswick

Rutgers, The State University of New Jersey

in partial fulfillment of the requirements

for the degree of

Master of Science

Graduate Program in Mechanical and Aerospace Engineering

written under the direction of

Professor Stephen D. Tse

and approved by

_____

_____

_____

New Brunswick, New Jersey

October 2009

ABSTRACT OF THE THESIS

INVESTIGATING LOCAL GROWTH CONDITIONS IN THE FLAME SYNTHESIS OF METAL-OXIDE NANOSTRUCTURES

By CASSANDRA D'ESPOSITO

Thesis Director:
Professor Stephen D. Tse

The synthesis of metal-oxide nanowires (i.e. $WO_{2.9}$, ZnO, Cu_2O, and Fe_3O_4) and nanoplates (i.e. MoO_2) is examined experimentally with metal-substrate probes inserted into counter-flow diffusion flames (CDFs) at atmospheric pressure. The quasi-one-dimensional flow field allows for correlation between morphologies and local growth conditions, as well as the tailoring of the flame structure, through computational simulations with detailed chemical kinetics and transport, to provide conditions suitable for gas-phase growth of nanostructures. Comparisons of products synthesized between methane and hydrogen flames, as well as between locations probed on either the fuel side or the air side of the reaction zone, permit evaluation of the roles of O_2 versus H_2O versus CO_2 in the oxidative route(s) involved. The as-synthesized nanostructures are characterized by field-emission scanning electron microscopy (FESEM), high-resolution transmission electron microscopy (HRTEM), and energy dispersive X-ray spectroscopy (EDXS).

Tungsten oxide nanowires are grown with diameters ranging from 50 to 200 nm at 1720K. The crystal structure is tetragonal $WO_{2.9}$, but the growth directions vary with flame conditions. Single-crystal ZnO nanostructures are formed at 1000, 1300, and

1600K. All growth mechanisms are possible based on Gibbs free energy calculations. Molybdenum oxide nanoplates are grown in the methane flame at 2000K on both the air and fuel sides, where similar amounts of H_2O and CO_2 are found. In the hydrogen flame, oxidized structures are grown on the air side, and micron sized plates are synthesized on the fuel side. Cu_2O nanowires are grown only on the air side of the methane and hydrogen flames, where large amounts of oxygen are present. The fuel sides of both flames show nucleation sites on the surface but no nanowire growth. Iron oxide nanowires are formed on the air side of the methane and hydrogen flames. Carbon nanotubes and nanowires are grown on the fuel side of the methane flame, while iron-oxide nodules are formed on the fuel side of the hydrogen flame.

ACKNOWLEDGEMENTS

I would like to thank my advisor, Professor Stephen Tse for his guidance on this project. Without him this would not have been possible, and I am grateful for all of his help. He always seemed to have a solution to the many obstacles I faced during my research. I also appreciate the time Prof. Lin and Prof. Pelegri spent reviewing and editing this work.

Many people have contributed to this work, and I am very thankful for their help. Dr. Fusheng Xu helped me understand this project and gave me insight into all of the experimental aspects of the research. Megan, it was nice to have another girl in the lab. We definitely figured out quite a bit about research together, and you helped me learn where everything is kept in the lab. Alex, thanks for always keeping the lab exciting and the trips we took to Princeton together. Thanks to Jon for keeping me company during many late nights working. Thanks to Xiaofei and Hadi for their laser diagnostics and analysis. Thank you Dr. Geliang Sun for your help with the materials science aspects of this project. I would like to thank Dr. Jafar Al-Sharab for his sample analysis and characterization on the TEM. Thanks to Prof. Greenhut and John Yaniero for their invaluable help and expertise in microscopy, as well as advice. Thanks to John Petrowski for his general knowledge in everything and his willingness to help solve any problem.

The financial support of the Army Research Office (through Grants W911NF-07-1-0425 and W911NF-08-1-0417), the National Science Foundation (through Grant CBET 0755615), and the Rutgers Mechanical and Aerospace Engineering Raisler Fellowship is gratefully acknowledged.

Finally, I would like to thank my family, who helped me immensely in too many ways to count. Thank you for the physical and emotion support and understanding during this. Thank you Mom, I never would have been able to do this without you.

LIST OF TABLES

LIST OF FIGURES

Chapter 1
Introduction

This thesis focuses on correlating local gas-phase growth conditions to resultant morphologies in the synthesis of various metal oxide nanostructures, such as $WO_{2.9}$, ZnO, MoO_2, Cu_2O, and Fe_3O_4. A review of synthesis conditions and materials properties are given within each specific metal-oxide chapter.

This chapter contains the motivation and objectives of this dissertation, as well as strategies and innovations in the field. Then a project overview is given followed by an outline of the ensuing chapters.

1.1 Motivation and Objective and Strategies

There are many ways to produce metal oxide nanostructures, for example, chemical vapor deposition, laser ablation, and arc discharge. Although the materials can be readily fabricated, very little is understood about the basic mechanisms involved in their formation. There are no known "universal" conditions that will produce a specific composition of nanowires, although conceptually they should exist. Flame synthesis has been shown to be a promising method for producing one-dimensional metal-oxide nanowires. Moreover, it can be fundamentally advantageous for controlling the key variables in nanostructure growth, such as gas-phase temperature and species concentrations. A counterflow diffusion flame (CDF) is a strategic flame that is easily probed for conducive conditions for nanowire growth that can be translated to other

geometries and even perhaps other gas-phase synthesis methods for larger-scale production.

To better understand the growth mechanisms producing the metal-oxide nanostructures, parametric studies comparing methane/air and hydrogen/air CDFs are conducted. The methane-based flame contains carbon, hydrogen, and oxygen species, with primary by-products H_2O and CO_2, while the hydrogen-based flame contains hydrogen and oxygen speices, with the by-product H_2O but no CO_2. Thus, hydrothermal (or hydrolysis) routes can be isolated. Furthermore, the CDF is quasi-one dimensional, with gradients existing only in the axial direction, allowing for meaningful simulations to be performed with detailed chemistry and transport. As a result, the gas phase temperatures and all of the relevant species concentrations at various positions within the flame can not only be determined (e.g. through Raman spectroscopy) but also tailored. In our studies, experiments are performed by probing two auspicious locations within a given flame for nanowire growth, where the temperatures are the same but where the chemical species concentrations are different (i.e. locations on the air side versus the fuel side of the exothermic flame reaction zone). Such a paradigm permits a rigorous uncovering of the fundamental growth mechanisms (e.g. O_2 vs CO_2 vs H_2O routes) of such nanomaterials synthesis.

There are many methods to produce nanostructures, namely CVD, laser ablation, arc discharge, and many others. The main objective of this work is to investigate the fundamental mechanisms involved in the gas-phase synthesis of metal-oxide nanostructures using well-defined flame synthesis. Some advantages to this process are

that high growth rates can be achieved on the order of microns per minute. The flame provides both the enthalpy and gas-phase reactants for synthesis to take place. No catalysts are needed because the nanowires grow directly on a metal substrate, and local conditions can be probed and identified. These experiments can be performed in ambient conditions; therefore, no expensive vacuum systems are necessary.

To correlate nanostructure characteristics with local growth conditions, parametric studies are performed using two different flame structures of different chemical composition, where the temperature profiles are purposely made the same. Therefore, the role of specific species can be isolated and assessed based on the resultant morphologies. Gibbs free energies are calculated for posited synthesis reactions to evaluate their contribution.

1.2 Overview

In this work, tungsten oxide, zinc oxide, molybdenum oxide, iron oxide, and copper oxide nanostructures are fabricated, and synthesis conditions are analyzed by employing the following method.

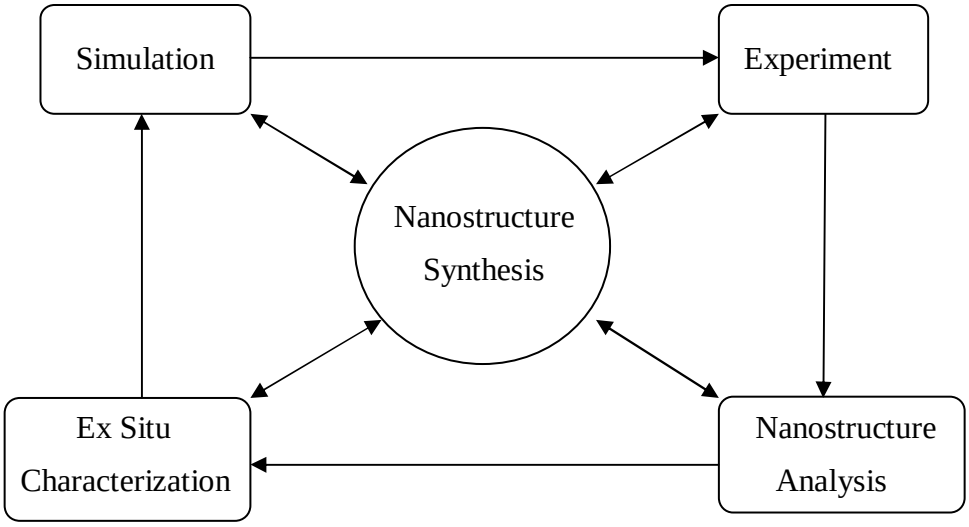

Figure 1.1 Flowchart of experimental method.

First, a simulation of the counterflow diffusion flame is performed in order to prescribe the flame structure, with appropriate temperature and species concentrations. The temperatures of the substrate are measured using an optical pyrometer. The CDF experiments are run with either methane or hydrogen as the fuel, and a parametric study is performed keeping temperature constant. The species concentrations, such as O_2, H_2O, and CO_2, are varied based on the flame configuration. The samples are then characterized using a scanning electron microscope (SEM) and a transmission electron microscope (TEM) to determine the morphology and structure of the synthesized metal-oxide nanomaterials. $WO_{2.9}$, ZnO, MoO_2, Fe_3O_4, and Cu_2O nanostructures of various morphologies are synthesized, and local growth conditions are determined.

$WO_{2.9}$ nanowires are grown on both the air and fuel side of the methane and hydrogen CDFs at locations corresponding to 1720 K from tungsten substrates. The air side of the

methane flame yields nanowires approximately 50 nm in diameter, while the air side of the hydrogen flame produces wires that are about four times as large. The fuel side of the methane flame produces thinner wires than does the air side. Again, the wires grown in the hydrogen flame have larger diameters than wires grown in the methane flame.

Many different ZnO nanostructures are produced by flame synthesis at various temperatures ranging from 1000 K to 1600 K. The largest number of morphologies are found when there is a comparable amount of CO_2, H_2O, and O_2 species present at the same location. The Gibbs free energies of the hypothesized reactions show that growth mechanisms involving all three species are possible to form ZnO nanowires.

MoO_2 nanostructures are grown from a molybdenum substrate at 2000K. On the air side and the fuel side of the methane flame, nanoplates are found; and H_2O and CO_2 are present in similar amounts. On the air side of the hydrogen flame, direct oxidation of the substrate surface seems to be taking place. On the fuel side of the hydrogen flame, micron sized plates are found, which are grown through a water vapor route.

Cu_2O nanowires are grown on the air side of the methane and hydrogen flame at 900 K, where oxygen is the dominant species present. On the fuel side, some oxidation patterns of the copper substrate is seen, but there is not enough to nucleate nanowires. Water vapor is the predominant species in this experiment, which indicates that oxygen is the only growth mechanism for copper oxide nanowire formation.

Magnetite (Fe_3O_4) nanowires are formed on the air side of the methane and hydrogen flames at 1000 K. Oxygen has the highest species concentration at the probed flame

location on the air side. On the fuel side of the methane flame, both carbon nanotubes (CNTs, formed catalytically from iron/iron-oxide nanoparticles) and iron oxide nanowires are formed. On the fuel side of the hydrogen flame, oxidation of the metal surface occurs, but no nanowires are formed. CO_2 and H_2O are present in the methane flame on the fuel side, and H_2O is present in the hydrogen flame on the fuel side. Therefore, CO_2 or CO plays the key role in CNT and metal oxide nanowire growth on the fuel side of the methane flame.

1.3 Outline of Thesis

Chapter 2 describes the experimental setups and procedures associated with the investigation of flame synthesis of nanowires. Chapter 3 explains the flame structure and governing equations, as well as the computational simulations performed. Chapter 4 examines the growth of tungsten oxide nanowires ,and the species required for growth. Chapter 5 correlates the local growth conditions with morphologies of as grown zinc oxide nanostructures. Chapter 6 investigates the growth conditions and morphologies of molybdenum oxide nanoplates. Chapter 7 evaluates the parametric studies performed to fabricate iron oxide and copper oxide nanowires. Finally, Chapter 8 presents conclusions and remarks on future work for the project. It should be noted that a brief literature review and background can be found in the beginning of each chapter for the specific metal-oxide nanostructure(s) investigated.

Chapter 2

Experimental Setup

2.1 Experimental setup configuration

In the experimental setup utilized to study the flame synthesis of metal-oxide nanomaterials, the main components are counterflow burners, mass flow controllers (MFCs) ,probe translator, cathetometer, and substrate probes. The burners produce a flat diffusion flame, and the MFCs controlled by a LabView program allow the flame to be tuned by producing accurate gas flow rates. The entire setup is housed in a Unistrut structure and mounted to a milling machine base. The translator and cathetometer allow the substrate probe to be accurately positioned to any point within the flame structure. Finally, the metal substrates must be prepared properly to be conducive for nanowire growth.

2.1.1 Counterflow burners

The counterflow diffusion flame consists of two opposing jets, the bottom one issuing fuel diluted with nitrogen gas and the top one issuing air. A stagnation plane is formed in between the opposing flows, and the fuel and oxidizer molecules mix through diffusion and form a flat flame above the stagnation plane,[1] given the stoichiometric ratios. An inert gas, such as nitrogen, is used as a co-flow in the burners to extinguish any outer flame, eliminate oxidizer entrainment, and reduce the amount of shear instabilities in the flame. The burners used in this setup are made of brass and each have a converging

nozzle with a 19 mm exit diameter and are positioned 15 mm apart. These burners are water-cooled to keep the brass from deforming and minimizing any flame instabilities. Below is a picture of the counterflow diffusion flame setup.

Figure 2.1 Actual image of CDF with methane flat flame.

2.1.2 Gas delivery setup

Mass flow controllers (MFCs) from Brooks Instruments are used to maintain the gas flow from the gas cylinders at a desired flow rate. The flow rate range of the MFCs used in this setup varies from 0-2 SLPM to 0-10 SLPM. A temperature difference is created in the MFC, which generates a linear 0-5 V signal that is directly proportional to the mass flow rate of the gas. The mass flow rates are controlled by a LabView program that has six outputs. This allows the user to choose a flow rate set point as a percent of full scale for each MFC.

Figure 2.2 Pictures of MFCs used in experiment.

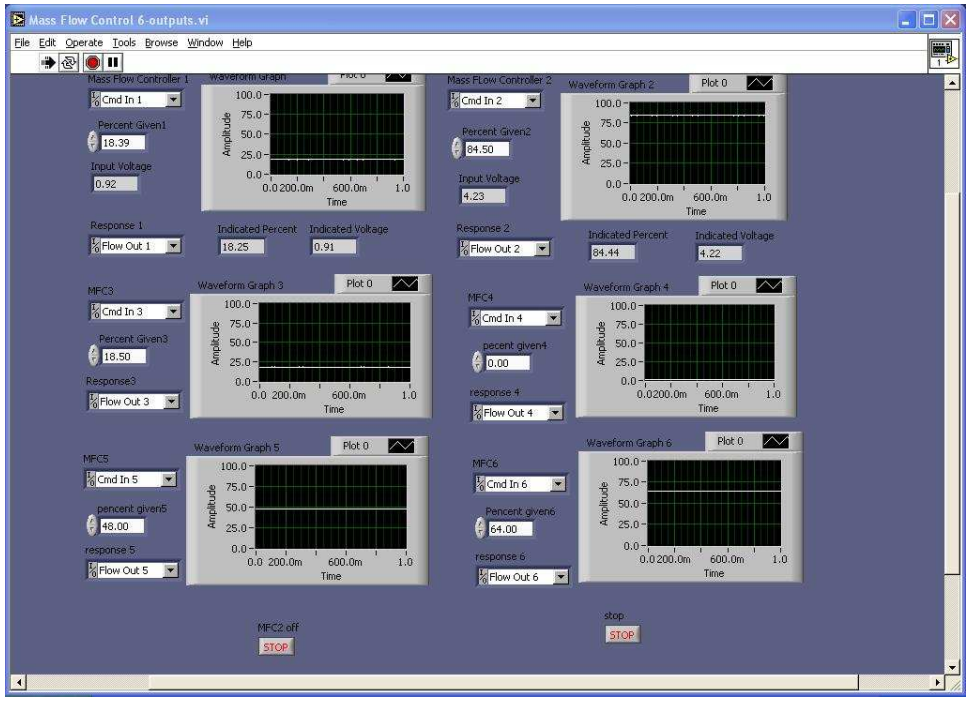

Figure 2.3 Screen image of LabView program used to control MFCs.

Below, Table 2.1, describes all of the MFCs with model numbers and flow rates used in the experiments. In Table 2.2, the gases along with the purity used are shown.

MFC	Model Number	Flow Rate Range (SLPM)
MFC 1	5850EMF3CAK2BKC	0-10
MFC 2	5850EME3CAMVEKC	0-2
MFC 3	5850EME3DAFRBKC	0-10
MFC 4	5850EMEZ41	0-2
MFC 5	5866RT	0-5
MFC 6	5866RB1J1B4Q2YC	0-5

Table 2.1 MFC data.

Gas	Purity
Hydrogen (H_2)	Pre-Purified Grade (99.99%)
Methane (CH_4)	CP Grade (99.0%)
Nitrogen (N_2)	High Purity (99.995%)

Table 2.2 Gas qualities.

2.1.3 Experiment housing

The entire experimental setup is mounted within a Unistrut enclosure. All sides around the burner are covered with plexi-glass in order to shield the flame from outside disturbances, such as cross flow. An exhaust hood is mounted above the enclosure so that combustion products and unburned gases from the flame are exhausted. This entire

setup is attached to a milling machine base, which serves as a 3-D translator to perform laser-based diagnostics for temperature and species concentration measurements.

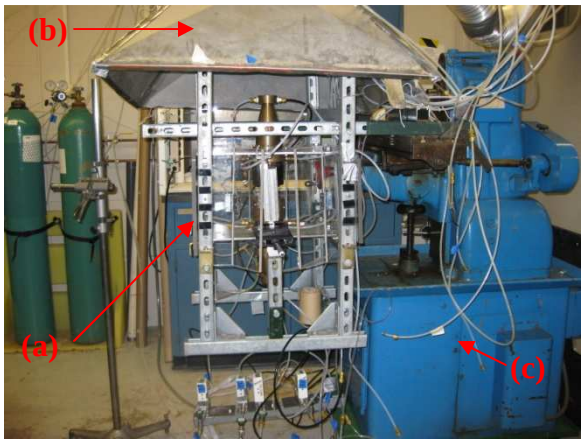

Figure 2.4 Experimental housing shown a) Unistrut support system with plexi-glass enclosures, b) ventilation hood, c) milling machine

2.1.4 Substrates

All of the substrates used are thin wires between 0.2 and 0.8 mm diameter, and the composition information is given in Table 2.3. Substrates are prepared by cutting all of the wires to a length of 63.5 mm. The ends are then marked by placing three scores 2 mm apart so that the growth areas can be identified with respect to them under characterization by the scanning electron microscope. Marked ends are placed in the flame for 10 minutes, after which they are placed with the cuts facing up on the microscope stud. Substrates are prepared carefully to ensure that no dirt, debris, or oxidation contaminates the wires. Prior to synthesis, all of the wires are sonicated in methanol to remove any impurities from the surface. The sonicator creates sound waves that travel through a fluid and remove any contaminants from the wire. Samples that can

oxidize, such as copper or iron, are first treated in a 10% nitric acid and water solution. The oxide layer of the sample usually has a higher melting point than the pure metal, which would prevent the substrate surface from evaporating and forming metal oxide nanowires.

Metal	Supplier	Diameter (mm)
99.98% Copper (Cu)	Omega Engineering, Inc.	0.2
99.9+% Iron (Fe)	Omega Engineering, Inc.	0.5
99.95% Molybdenum (Mo)	McMaster-Carr	0.8
99.95% Tungsten (W)	Small Parts, Inc.	0.8
Zinc galvanized steel (Zn)	McMaster-Carr	0.8

Table 2.3 Substrate diameters and suppliers.

2.1.5 Three-axis translator and cathetometer

To properly position the substrate within the flame structure, a three-axis translator is used in the experiment. The vertical position of the substrate must be varied to expose the substrate to a specified temperature. Also, the tip of the substrate must be at the center of the flame to guarantee the most accurate results. The substrate height above the bottom burner is verified with a cathetometer that has a resolution of 0.5 mm. First, the cathetometer is leveled at the base and the viewing area, and then it is focused. Then, the height of the bottom burner is measured and the proper flame height is confirmed. It must be noted that the view in the cathetometer is inverted. Finally, the cathetometer is set to the designated distance away from the flame on the air or fuel side.

Figure 2.5 Three axis translator (left) and cathetometer (right).

2.2 Operating conditions and procedures

Descriptions of the standard operating procedures for the methane and hydrogen diffusion flames are given below.

2.2.1 Experimental procedure for methane counterflow diffusion flame

(1) Make sure the setup is under a ventilation hood, and turn on the roof fan.

(2) Turn on the compressed air and check the pressure gage, and make sure it is set to 20 psi.

(3) Turn on the methane and nitrogen cylinders, then set the pressure regulators to 20 psi, and finally open the valve next to the regulator.

(4) Turn on the cooling water, and adjust the valve until the cooling water does not cause condensation on the burner.

(5) Open the LabView program for 6 outputs, and input the correct values.

(6) For the 50% CH_4 and 50% N_2 flame, make the following settings.

a. MFC 1: methane at 1.32 L/min

b. MFC 2: nitrogen to dilute methane at 1.32 L/min

c. MFC 3: air at 2.58 L/min

d. MFC 4: not used in this flame

e. MFC 5: nitrogen co-flow on the fuel side at 2.4 L/min

f. MFC 6: nitrogen co-flow on the air side at 3.2 L/min

(7) For the 100% CH_4 flame, make the following settings.

a. MFC 1: methane at 2.64 L/min

b. MFC 2: not used in this flame

c. MFC 3: air at 2.58 L/min

d. MFC 4: not used in this flame

e. MFC 5: nitrogen co-flow on the fuel side at 2.4 L/min

f. MFC 6: nitrogen co-flow on the air side at 3.2 L/min

(8) Turn on the valves upstream of the mass flow controllers (MFCs).

(9) Turn on the power to the MFCs.

(10) Click the RUN button in LabView.

(11) Ignite the flat flame.

(12) Set up and level the cathetometer.

(13) Adjust cathetometer cross-hairs so that the horizontal line is even with the bottom burner.

(14) Then check that the flame is at the correct height.

(15) Raise the horizontal line to the correct level that corresponds to the correct temperature.

(16) Insert the substrate into the 3-axis translator and adjust the height of the substrate.

(17) Make sure that the tip of the substrate is at the center of the flame.

(18) Leave the substrate in the flame for 10 minutes.

(19) Remove the sample and cut off substrate so it fits on the SEM stud.

(20) Place sample on an SEM stud covered with carbon tape and examine under the FESEM.

(21) When finished, turn off the methane cylinder, and let the flame burn out completely.

(22) Turn off the nitrogen, air, and water.

(23) Shut off the power to the MFCs, and close the LabView program.

(24) Close all of the valves upstream from the MFCs.

(25) Turn off the roof ran.

2.2.2 Experimental procedure for hydrogen counterflow diffusion flame

(1) Make sure the setup is under a ventilation hood, and turn on the roof fan.

(2) Turn on the compressed air, check the pressure gage, and make sure it is set to 20 psi.

(3) Turn on the hydrogen and nitrogen cylinders, then set the pressure regulators to 20 psi, and finally open the valve next to the regulator.

(4) Turn on the cooling water ,and adjust the valve until the cooling water does not cause condensation on the burner.

(5) Open the LabView program for 6 outputs, and input the correct values.

(6) For the 36.5% H_2 and 63.5% N_2 flame, make the following settings.

   a. MFC 1: nitrogen to dilute hydrogen at 2.13 L/min
   b. MFC 2: hydrogen at 1.23 L/min
   c. MFC 3: air at 2.72 L/min
   d. MFC 4: not used in this flame
   e. MFC 5: nitrogen co-flow on the fuel side at 2.4 L/min
   f. MFC 6: nitrogen co-flow on the air side at 3.2 L/min

(7) For the 44.0% H_2 and 56.0% N_2 flame, make the following settings.

   a. MFC 1: nitrogen used to dilute hydrogen at 1.88 L/min
   b. MFC 2: hydrogen at 1.48 L/min
   c. MFC 3: air at 2.72 L/min
   d. MFC 4: not used in this flame
   e. MFC 5: nitrogen co-flow on the fuel side at 2.4 L/min
   f. MFC 6: nitrogen co-flow on the air side at 3.2 L/min

(8) Turn on the valves upstream of the mass flow controllers (MFCs).

(9) Turn on the power to the MFCs.

(10) Click the RUN button in LabView.

(11) Ignite the flat flame, and turn off the lights in order to see the flame.

(12) Set up and level the cathetometer.

(13) Adjust cathetometer cross-hairs so that the horizontal line is even with the bottom burner.

(14) Check that the flame is at the correct height.

(15) Raise the horizontal line to the correct level that corresponds to the correct temperature.

(16) Insert the substrate into the 3-axis translator, and adjust the height of the substrate.

(17) Make sure the tip of the substrate is at the center of the flame.

(18) Leave the substrate in the flame for 10 minutes.

(19) Remove the sample and cut off substrate so it fits on the SEM stud.

(20) Place sample on an SEM stud covered with carbon tape and examine under the FESEM.

(21) When finished, turn off the methane cylinder, and let the flame burn out completely.

(22) Turn off the nitrogen, air, and water.

(23) Shut off the power to the MFCs, and close the LabView program.

(24) Close all of the valves upstream from the MFCs.

(25) Turn off the roof ran.

2.3 Ex-situ characterization methods

2.3.1. Field emission scanning electron microscope (FESEM)

A scanning electron microscope (SEM) can be used for nanoscale imaging because it can magnify up to 200,000X. A LEO Zeiss Gemini 982 is used to determine the morphologies of the as-grown nanostructures at magnifications between 3,000X and 20,000X. The length and diameter of nanowires can be determined as well. The substrate is mounted on a stud using conductive carbon tape so that no charging effects are manifested. Then the sample must be desiccated for twenty-four hours prior to insertion into the microscope due to the high vacuum requirements of the FESEM chamber.

2.3.2 Transmission electron microscope (TEM)

The structural features of the nanomaterials are determined using a high resolution transmission electron microscope (HRTEM). The crystallinity and composition of the samples can be determined using selected area electron diffraction (SAED), which is a feature of the TOPCON 002B HRTEM. The samples are sonicated in ethyl alcohol and the resulting solution is dispensed onto a holey or lacey carbon grid using a pipette. The prepared grids are then viewed in the microscope.

2.3.3 Energy dispersive x-ray spectroscopy (EDXS)

The TEM and FESEM are able to perform EDXS in order to determine the elements present within a sample. Therefore, the composition of the nanomaterials can be verified as metal oxides.

Chapter 3

Flame Structure

3.1 Flame Structure

To produce metal-oxide nanomaterials, certain local parameters, including temperature and species concentrations, need to be specified. A counterflow diffusion flame[1] is utilized in this experiment because it is a well-defined system that can be easily tailored to produce a local environment that is conducive to nanowire growth. The flow field produces a flat flame that is quasi one-dimensional, with gradients only in the axial *z*-direction, allowing the flame structure to be modeled using computational simulations with detailed chemical kinetics and transport properties.

A schematic of the flow field with the stagnation plane and the flame is shown in

Figure **3.1**. An actual flame can be seen in Figure 3.2. The top burner issues the oxidizer, and the bottom jet issues the fuel. A stagnation plane is formed in between the jets, the location of which depends on the momentum fluxes of the fuel and oxidizer. The flame is situated at a plane on the oxidizer side of the stagnation plane where the conditions are stoichiometric. The flame formed by the two nozzles is a flat disk in shape. The flat flame only has temperature, T, mass fraction, Y_k, and velocity, u, that varies in the z direction. The velocity, v, varies in the radial direction.

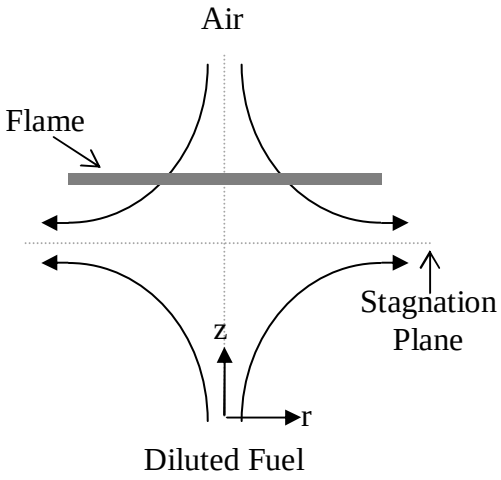

Figure 3.1 Schematic of flow field established with CDF.

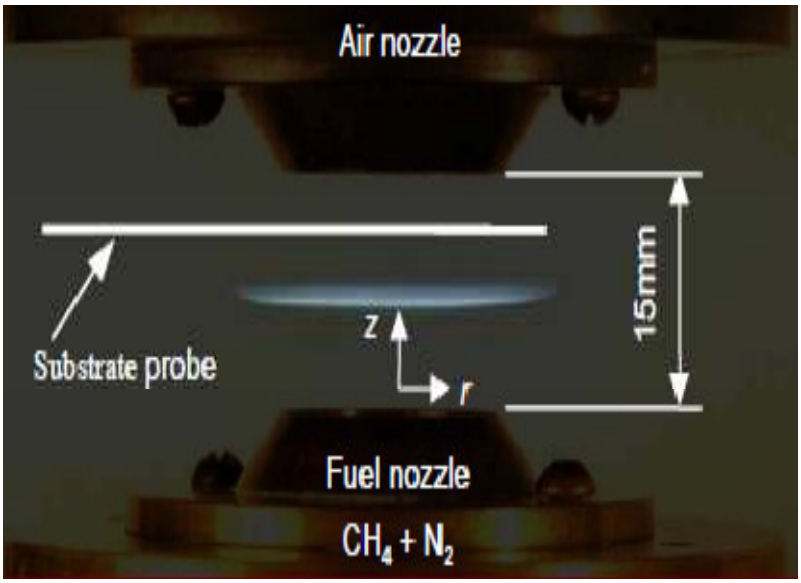

Figure 3.2 Picture of flate flame.

3.2 Simulation

To solve the mathematical equations, a boundary-value problem of ordinary differential equations is solved using an in-house code called Dif.f., originally modified by Prof.

Yiguang Ju, presently at Princeton. First, the stream function, $\varphi = r^2 U(z)$, is utilized to transform the governing equations, where *U(z)* is the mass flux. The partial derivitaves of the stream function give the following equations, where ρ is the density of the mixture, *u* is the axial velocity, and *v* is the radial velocity.

$$\frac{\partial \varphi}{\partial r} = r\rho u = 2rU \tag{3.1}$$

$$-\frac{\partial \varphi}{\partial z} = r\rho v = -r^2 \frac{\partial U}{\partial z} \tag{3.2}$$

The stream function then satisfies the mass continuity equation as shown below.

$$\frac{\partial}{\partial z}(r\rho u) + \frac{\partial}{\partial r}(r\rho v) = 0 \tag{3.3}$$

By using a substitution for reduced velocity where $G(z) = \frac{v}{r}$, the mass conservation equation becomes

$$\frac{dU}{dz} + \rho G = 0 \tag{3.4}$$

.

The conservation of momentum equation using the previous assumptions and the equation $J = \frac{1}{r}\frac{\partial p}{\partial r}$, where *p* is the thermodynamic pressure, is given below in Eq. 3.5. The derivative $\frac{\partial J}{\partial z} = 0$, and μ is the viscosity of the gaseous mixture.

$$\frac{d}{dz}\left(\mu \frac{dG}{dz}\right) - 2U\frac{dG}{dz} + J - \rho G^2 = 0 \tag{3.5}$$

The species equation for all k species can be expressed

$$2U\frac{dY_k}{dz} + \frac{d}{dz}(\rho Y_k V_k) - W_k \dot{\omega}_k = 0 \quad for\ k = 1 - K \quad . \tag{3.6}$$

In the above equation, V_k is the diffusion velocity of the k^{th} species, W_k the molar mass of the k^{th} species, and $\dot{\omega}_k$ the molar rate of production for the chemical reactions of the k^{th} species.

Lastly, the conservation of energy equation is given as

$$2U c_p \frac{dT}{dz} - \frac{d}{dz}\left(\lambda \frac{dT}{dz}\right) + \left(\sum_{k=1}^{K} \rho Y_k V_k c_{pk}\right)\frac{dT}{dz} + \sum_{k=1}^{K} h_k W_k \dot{\omega}_k) = 0. \tag{3.7}$$

where c_p is the specific heat of the mixture, λ the thermal conductivity of the gas mixture, c_{pk} the specific heat of the k^{th} species, and h_k the specific molar enthalpy of the k^{th} species.

The four differential equations can be solved as long as boundary conditions are prescribed. The conditions and $z = 0$ and $z = L$ are given below.

$z = 0$: $$U = \frac{\rho_o u_o}{2}, \qquad G = 0, \qquad T = T_o, \qquad Y_k = Y_{ko} \tag{3.8}$$

$z = L$: $$U = \frac{\rho_L u_L}{2}, \qquad G = 0, \qquad T = T_L, \qquad Y_k = Y_{kL} \tag{3.9}$$

All of the chemical kinetics and transport (λ, μ), along with thermodynamic properties (c_p, c_{pk}, h_k), are calculated using CHEMKIN[2] and TRANPORT[3] subroutines called by the Dif.f code. For the methane/air combustion, the kinetic mechanism of GRI-Mech 1.2[4] is used. For hydrogen/air combustion, the kinetic mechanism of Meuller *et al.*[5] is

employed. The Dif.f code solves the governing equations using the given boundary conditions. All of these parameters, such as flow velocities and species concentrations, are specified by using an input file. A "guess" solution can be given as input by using a restart file, and the new converged solution is given in the output file.

3.3 Simulation Results

The simulations can be run for many different flame configurations where the reactants and flow velocities are varied. The flame structures and velocities used in the simulations are shown in Table 3.1 below. The first two cases are employed for the experiments with tungsten, zinc, iron, and copper as substrates. The last two cases are utilized where a higher temperature is needed for the molybdenum experiments. The first two flame configurations have temperature profiles that are purposely matched and can be seen in Figure 3.3, so that the effect of species concentrations can be compared. The last two flame structures are strategically matched as well, which is shown in Figure 3.4.

Flame Type	Percentages Fuel Side	Velocity Air Side (cm/s)	Velocity Fuel Side (cm/s)
Methane	50% CH_4 and 50% N_2	-15.07	15.44
Hydrogen	36.5% H_2 and 63.5% N_2	-16.00	19.75
Methane	100% CH_4	-15.07	15.44
Hydrogen	44.0% H_2 and 56.0% N_2	-16.00	19.75

Table 3.1 Flame simulation information.

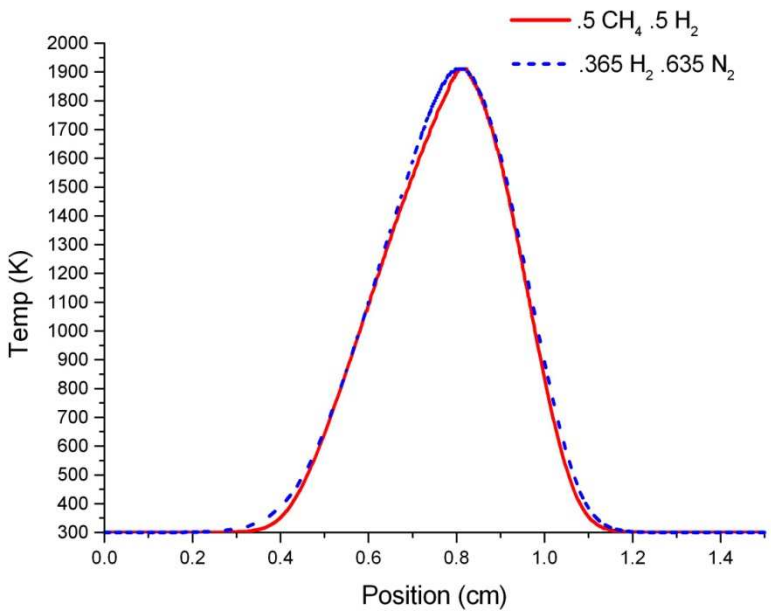

Figure 3.3 Temperature profiles for 50% methane diluted with 50% nitrogen and 36.5% hydrogen diluted with 63.5% nitrogen.

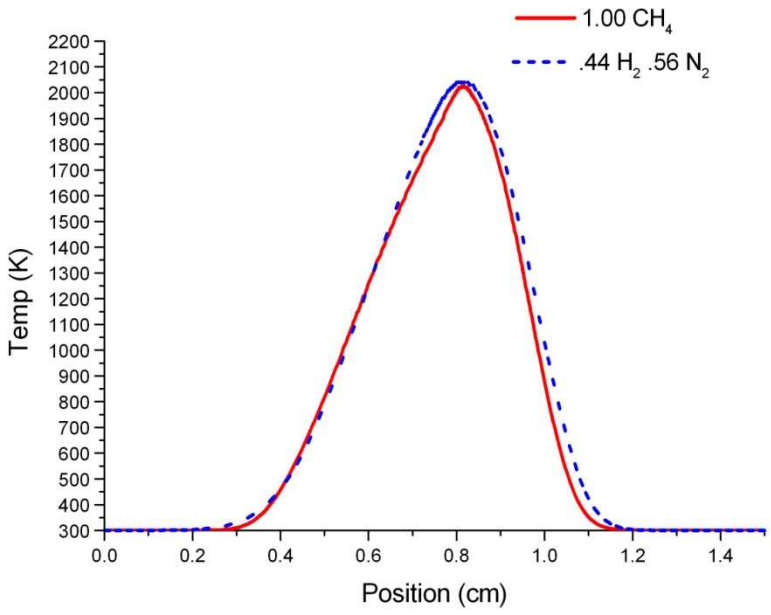

Figure 3.4 Temperature profiles for 100% methane and 44% hydrogen diluted with 56% nitrogen.

All of the simulation results can be seen in the graphs below. The first graph shows the temperature and velocity profiles. The stagnation plane on the graph is the location where the velocity is equal to zero. This shows that, for our cases, all of the flames are formed on the air side of the stagnation plane. The second graph shows the relevant species concentrations within the flame. The simulations allow us to tailor the experimental flame to provide the local conditions to be probed, and laser-based Raman spectroscopy of the flame structure then validates them.

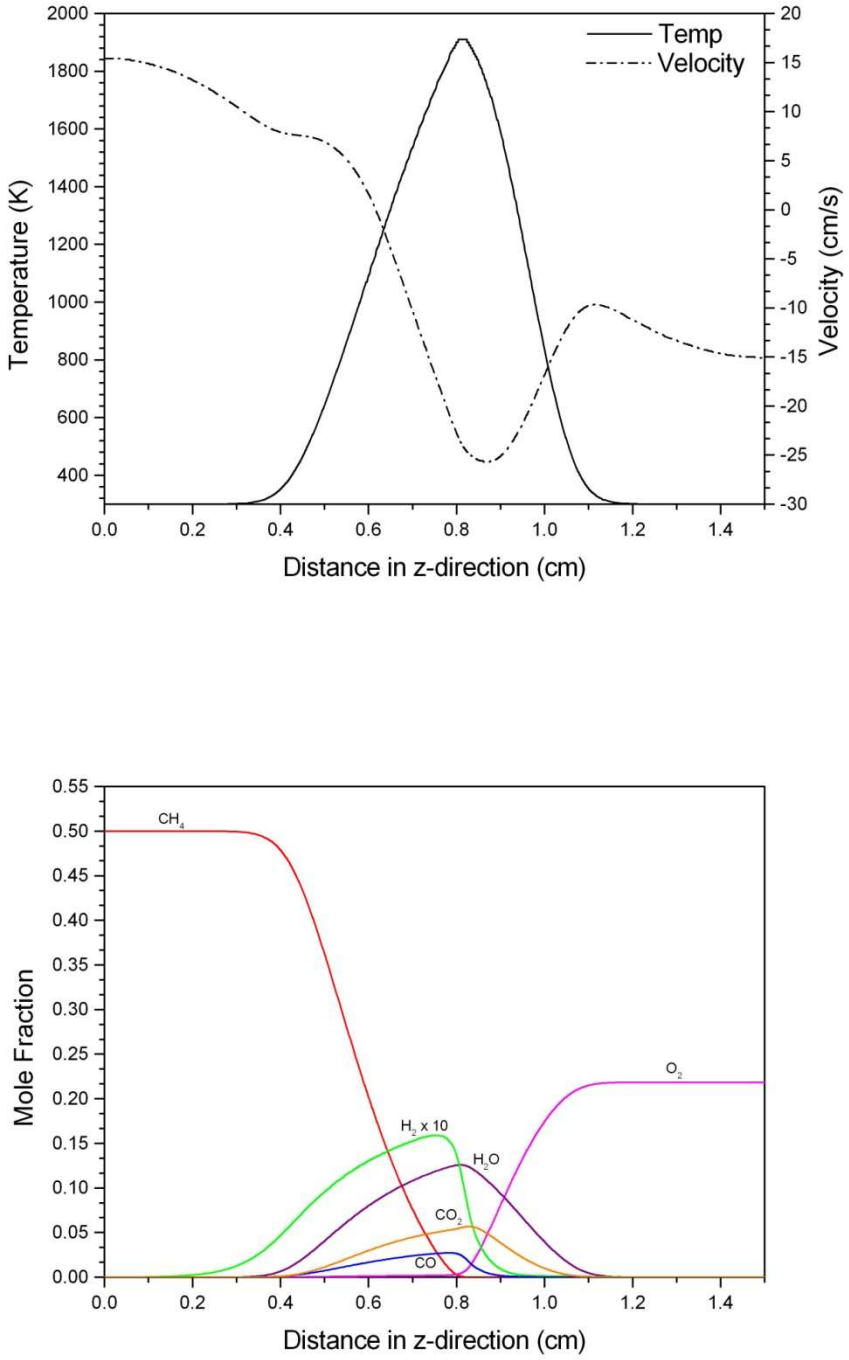

Figure 3.5 Methane simulation results for 50.0% CH_4 and 50.0% N_2 a) temperature and velocity profiles b) species concentration in mole fraction.

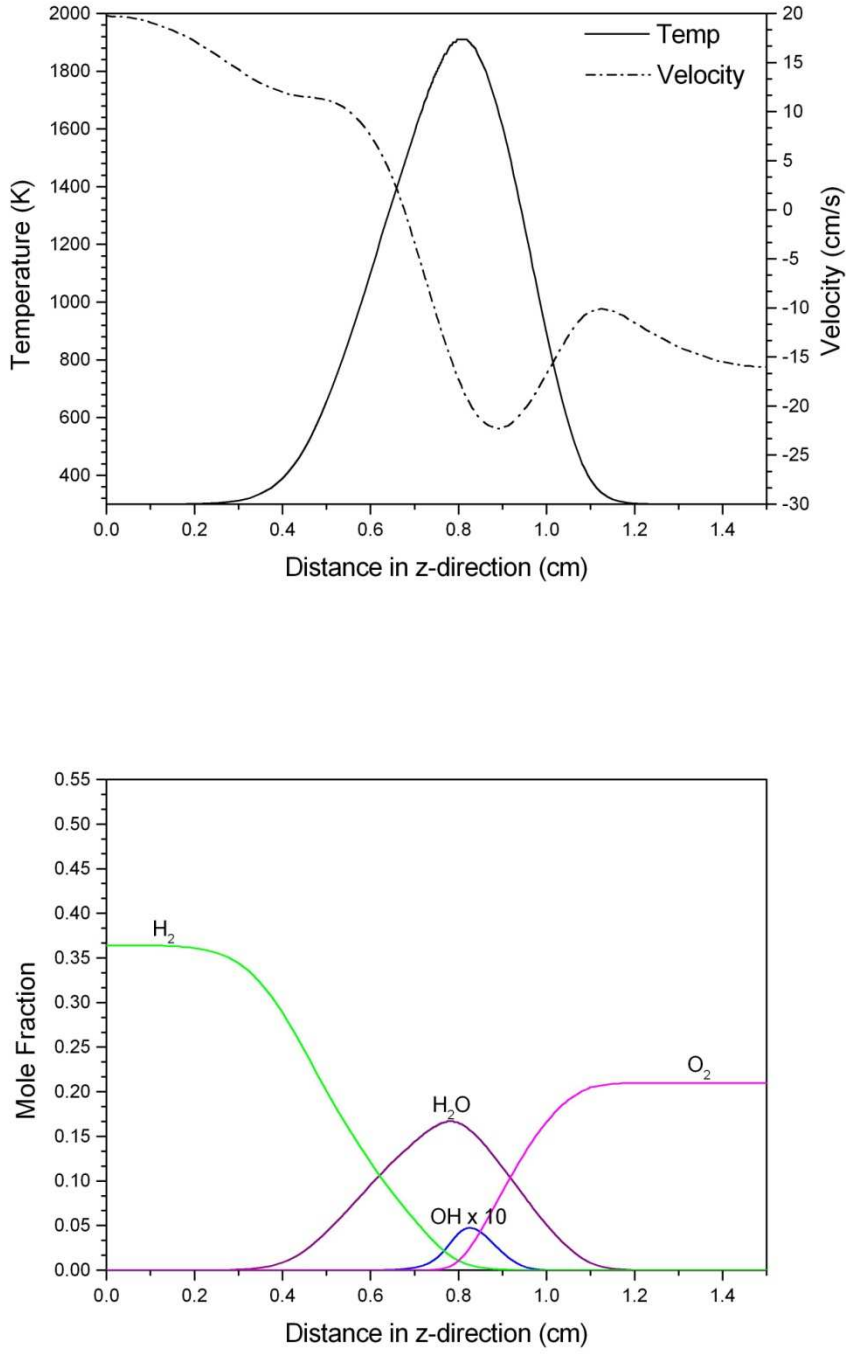

Figure 3.6 Hydrogen simulation results for 36.5% H_2 and 63.5% N_2 a) temperature and velocity profiles b) species concentration in mole fraction.

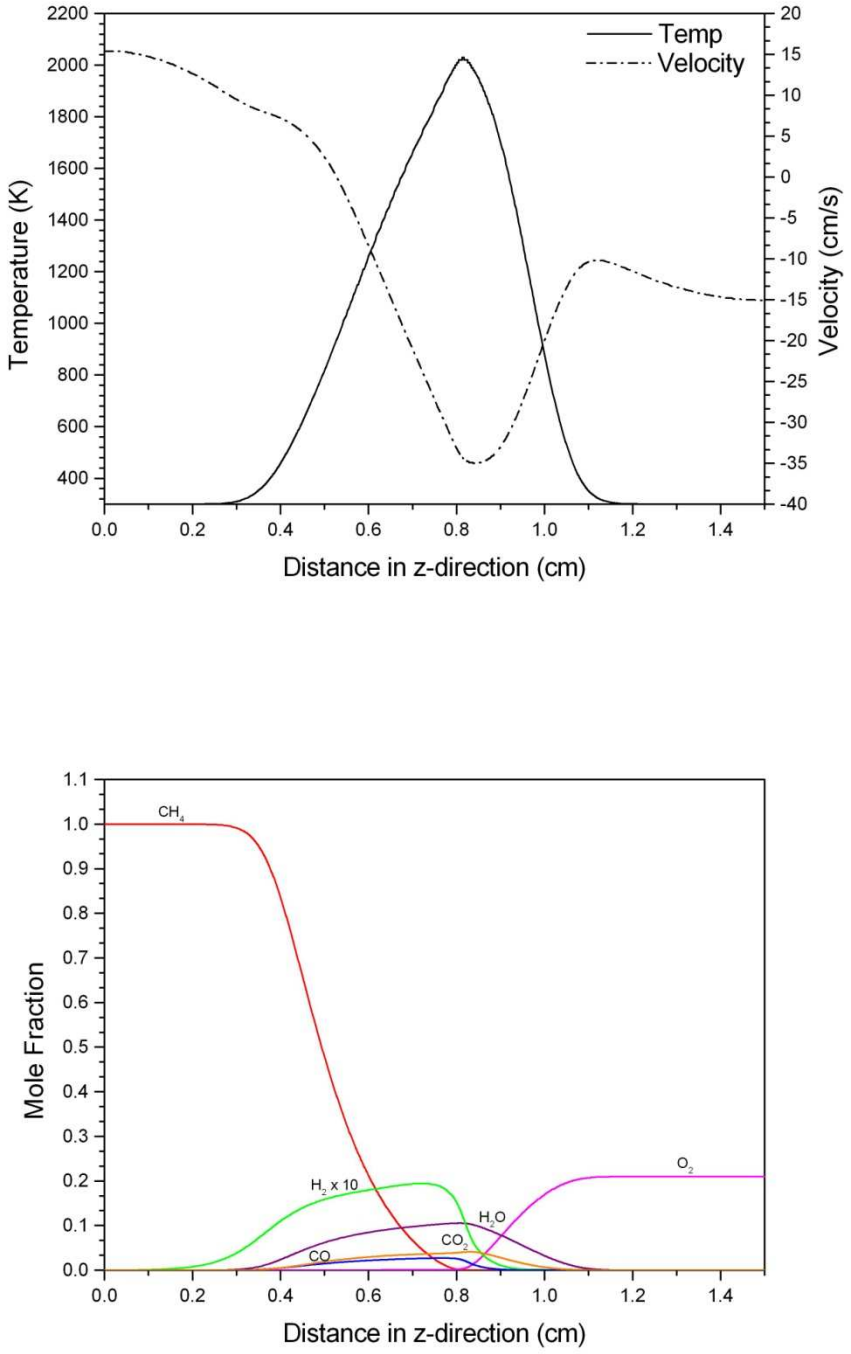

Figure 3.7 Methane simulation results for 100.0% CH_4 a) temperature and velocity profiles b) species conentration in mole fraction.

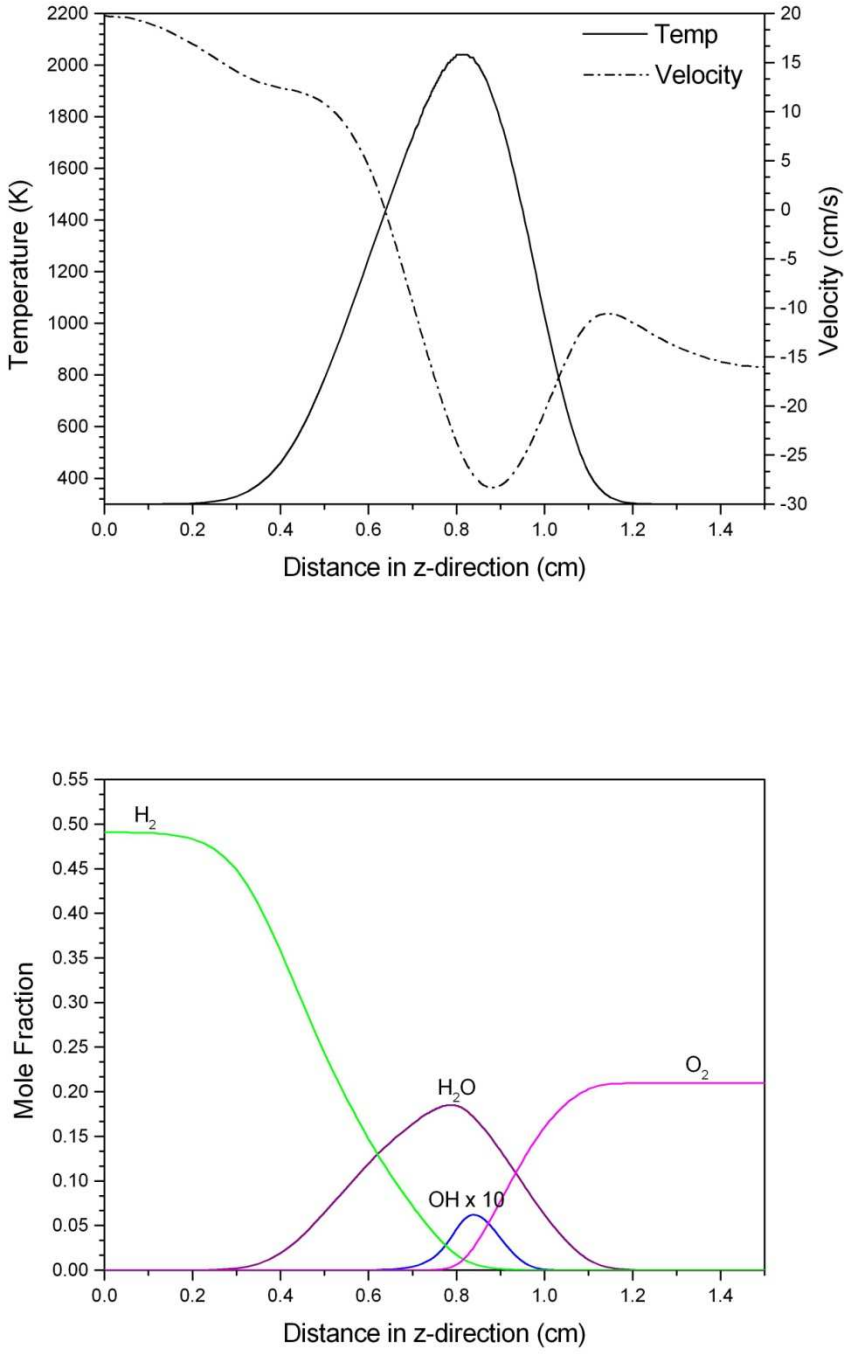

Figure 3.8 Hydrogen simulation results for 44.0% H_2 and 56.0 N_2 a) temperature and velocity profiles b) species concentration in mole fraction.

Chapter 4

Tungsten Oxide Nanowires

Tungsten oxide is an n-type semiconductor with fascinating properties in the fields of electrochromic devices, selective catalysts both for oxidation and reduction reactions, and gas sensors. Tungsten oxide nanostructured thin films have been tested, displaying superior sensitivity compared to bulk materials. However, studies on nanoscale WO_x materials, as well as their applications, are presently limited due to lack of easy processes for high- rate, yield, purity, and orientation synthesis for them. The growth of nanowires over large areas remains especially challenging. Ostensibly, there is much to be investigated about the dependence between the synthesis conditions and morphologies.

In this work, various WO_x nanostructures are produced in counterflow diffusion flames, which are well-suited for correlation of morphologies with local conditions. The synthesis is carried out at atmospheric pressure using tungsten metal wires as substrates. The axial separation of fuel side and air side with respect to the reaction zone permits evaluation of the roles of H_2O versus CO_2 versus O_2. Laser-based diagnostics are used to map local chemical species concentrations and gas-phase temperature with WO_x growth morphology, helping to divulge the growth mechanisms. These are compared with computational simulations and show good agreement. Comparisons of tungsten oxide morphologies and compositions synthesized in methane and hydrogen flames allows for assessment of the respective roles of H_2O versus CO_2 versus O_2.

4.1 Introduction

In recent years, the remarkable properties of metal oxide nanowires have gained attention in the scientific community. In particular, tungsten oxide nanomaterials can be utilized for their electrochromic, optochromic, gaschromic, and magnetic properties. They can be used in various sensors, flat panel displays, "smart" windows, and optical devices. Many different methods have been developed to produce tungsten oxide nanomaterials with varying morphologies, such as tree-like structures, nanowires, nanparticles, and nanotubes.[6-18] Vapor-solid and vapor-liquid-solid are among the main growth methods to produce them. If KI is used as a catalyst in the formation of tungsten oxide, a liquid phase usually exists which causes a vapor-liquid-solid growth mechanism to be present.[7,8] Hong *et al.*[8] described a growth mechanism where water vapor and oxygen gas reacted with tungsten in order to form WO_3. The water helped to generate highly mobile substances, such as hydrate species, which are precursors for WO_3 nanoribbon formation. If WO_3 is evaporated, tungsten oxide can be formed through the vapor-solid method when the vapor recondenses.[9,10] Gu *et al.*[11] heated tungsten tips, and small tungsten oxide particles were able to mobilize on the substrate surface and create nucleation sites for the nanowires. Tungsten powder can also be evaporated and condensed with residual oxygen producing tungsten oxide nanowires through the vapor-solid mechanism.[12] Jin *et al.*[13] proposed that tungsten reacted with water in order to produce WO_x. They proposed a direct and indirect growth method for forming WO_x ($2.5 \leq x \leq 2.9$) nanoneedles. In the direct route, tungsten combined with water vapor to produce WO_x, and in the indirect route an intermediate WO_3 is formed which then reacts with hydrogen to produce WO_{3-x}. Rothschild *et al.*[14] investigated the morphology of WOx nanowires grown in the presence

of water vapor and oxygen. Needlelike wires were formed when water vapor was introduced, but spherical particles were grown with the oxygen route. This proved that hydrogen played a role in the morphology of the as grown $WO_{2.9}$ needlelike particles. Viddiraju *et al.*[15] calculated the Gibbs free energies for the reactions between tungsten and oxygen to form WO_2 and WO_3 and concluded that the reactions were indeed spontaneous.

Many of these methods require the use of expensive vacuum systems, but our flame synthesis experiment can be performed in ambient conditions.[9,16,17,18,19] Also, pretreatment and catalysts are necessary for many processes described above, yet in flame synthesis, the tungsten oxide nanowires grow directly on a tungsten substrate.[8,20,21,22,23] Presently, further studies on WO_x nanomaterials applications are restricted by the inadequate processes for high growth rates, purity, and orientation. Therefore, in this work parametric studies are employed in order to correlate WO_x morphologies and local growth conditions, revealing growth mechanisms. Hydrogen and methane counterflow diffusion flames (CDFs) are probed with tungsten substrate probes at different locations (but the same gas-phase temperature) on the air and fuel sides of the reaction zone. Voltage bias is applied to the wires to investigate electric field effects on the morphology.

4.2 Experiment

The CDF setup consists of two converging nozzles with 19 mm diameter and 15 mm separation distance (Figure 4.2). The top burner issues air, and the bottom burner issues either diluted-methane (50% N_2 / 50% CH_4) or diluted-hydrogen (63.5% N_2 / 36.5% H_2).

A nitrogen co-flow extinguishes any outer flame, minimizes shear instabilities, and eliminates oxidizer entrainment.

The CDF is utilized due to its quasi one-dimensionallity, which allows the chemical species to be tailored according to certain specifications by performing computational simulations. The temperature profiles of the methane and hydrogen flames have been strategically matched in order to compare chemical species. Figure 4.1 shows graphs of the temperature and species concentration profiles of the two flame structures obtained by computational simulations using GRI-Mech 1.2,[4] and confirmed by spontaneous Raman spectroscopy (SRS), as shown in the Figure 4.2(b).

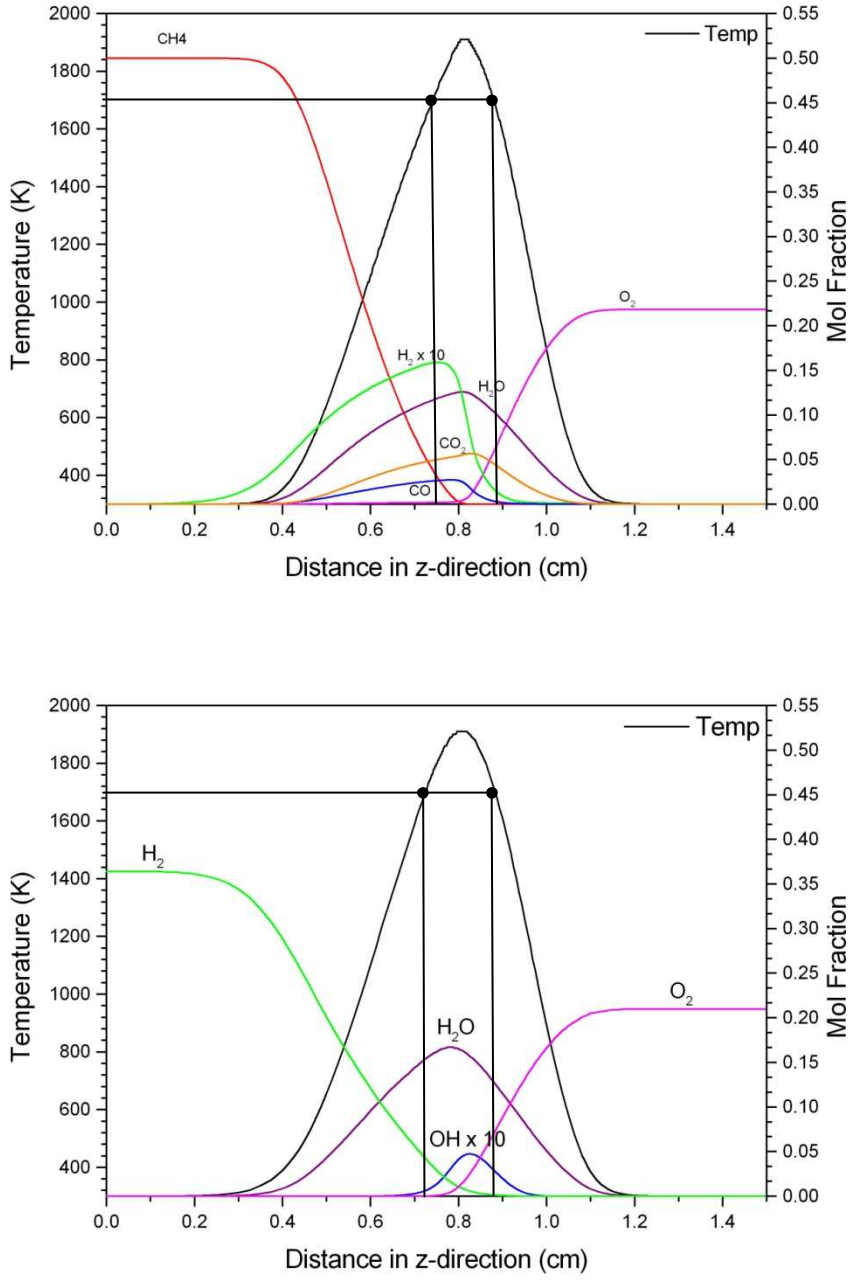

Figure 4.1 Gas phase flame structure of methane and hydrogen flames.

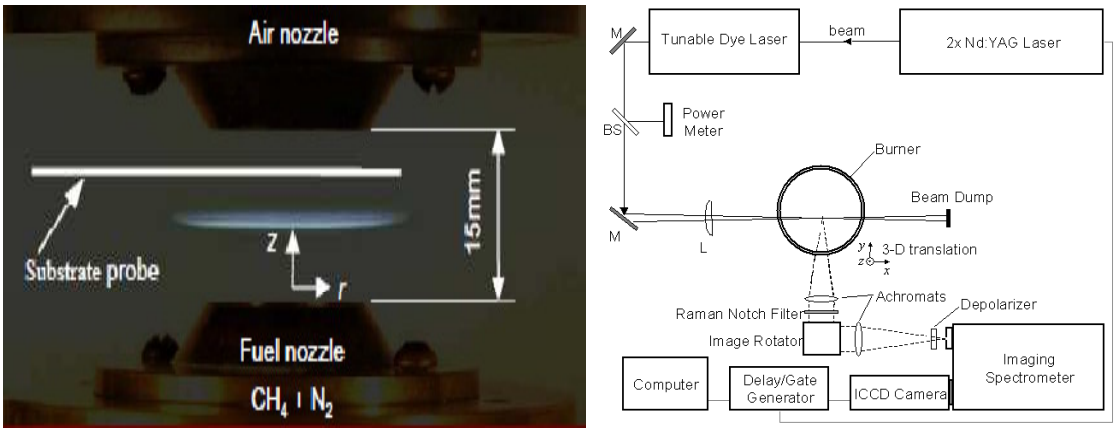

Figure 4.2 (a) Counterflow diffusion flame utilized in experiment. (b) SRS diagnostic setup.

An ultrasonically-cleaned tungsten substrate is inserted into the CDF at a position either on the air side or the fuel side of the flame in ambient conditions where the gas temperature is ~1720K for 10 minutes (see Figure 4.1). Using a pyrometer, the substrate temperature is estimated to be ~1400K . The morphologies of as-grown nanostructures are examined using field emission scanning electron microscopy (FESEM, LEO Zeiss Gemini 982). Structural features of the nanomaterials are investigated using high resolution transmission electron microscopy (HRTEM, TOPCON 002B), along with selected area electron diffraction (SAED).

4.3. Results and Discussion

4.3.1 Air-Side

Tungsten oxide nanowires are grown in all of the probed locations in the flame. The species concentrations vary at each location; therefore, it is possible to relate local growth conditions to nanowire morphologies. Images of the nanowires grown on the air side of the methane diffusion flame show a dense yield of nanowire bundles in Figure 4.3(a) and

(b). The wires are approximately 50 nm in diameter and 2 µm in length. On the air side of the hydrogen flame, the wires are thicker and longer than the wires grown in the methane flame. These wires have diameters of about 200 nm and lengths >10 µm. They also are not well aligned as can be seen in Figure 4.4(a) and (b).

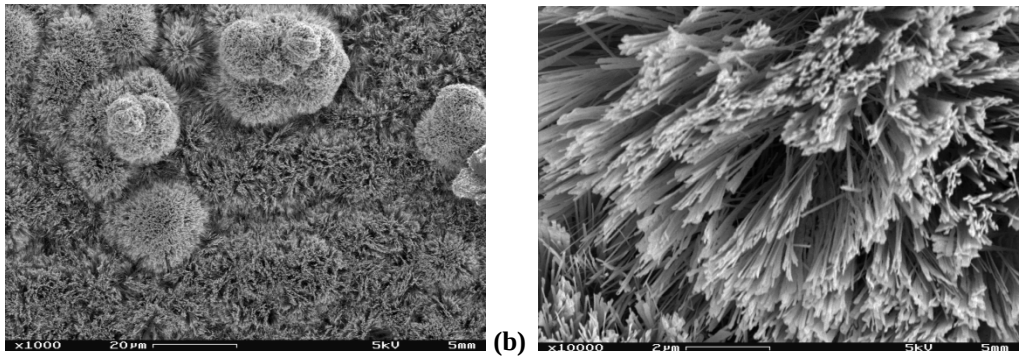

Figure 4.3 (a) Low magnification tungsten oxide nanowires grown in a CH_4 flame (b) Magnified FESEM image of nanowires grown in CH_4

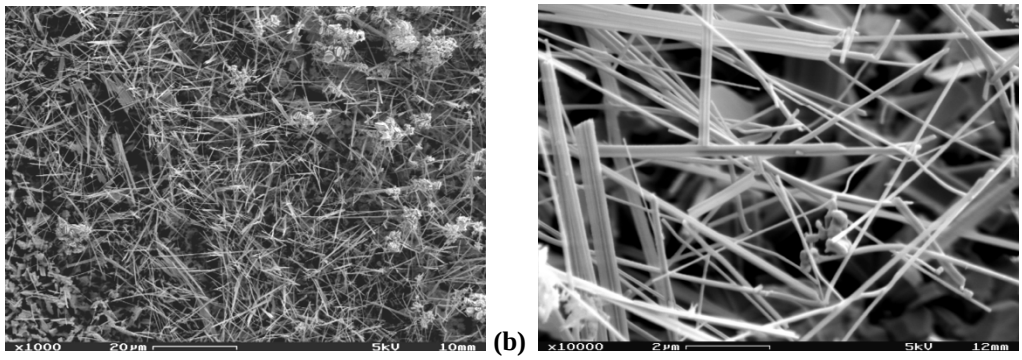

Figure 4.4 (a) Low magnification showing dense yield of tungsten oxide from H_2 flame (b) Typical image of tungsten oxide grown in the H_2 flame

On the air side in the methane and hydrogen flames, $WO_{2.9}$ is confirmed from the SAED pattern. Below, in Figure 4.5(a) is a TEM image of a 190 nm $WO_{2.9}$ nanorod, with the diffraction pattern shown as in the inset that is grown on the air side of the hydrogen flame. The 90° branching of the nanorods, shown in Figure 4.5(b), is due to the similar d-spacings in the [1,1,0] and [-1,1,0] directions.

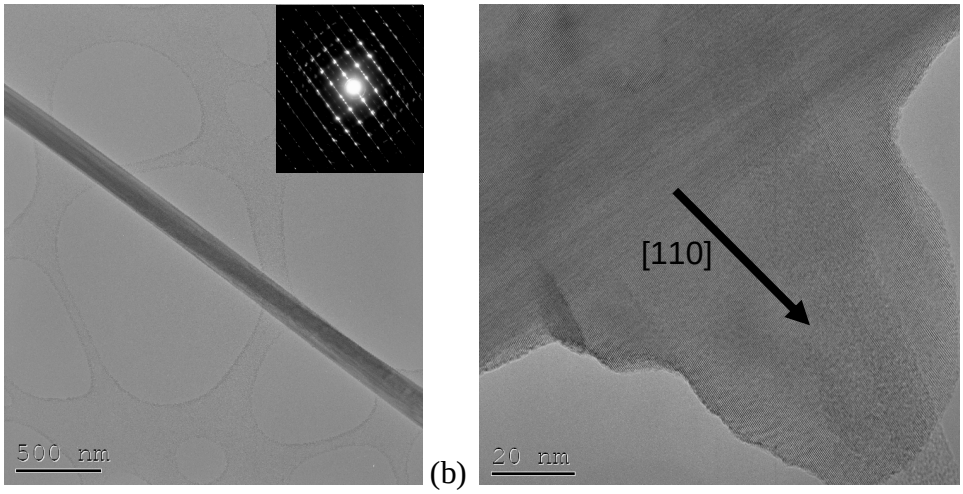

Figure 4.5 (a) TEM image of $WO_{2.9}$ nanorod with SAED pattern in upper right corner (b) Branching in the [1,1,0] growth direction

The concentrations of the gas species are shown in Table 4.1, for the air side of the methane and hydrogen flames. At 1720 K, the temperature is sufficient to vaporize tungsten/oxygen species from the substrate, and allow them to react with oxygen gas on the air side of the reaction zone. A vapor-solid growth route is most probable, and small WO_x particles formed on the substrate may nucleate the WO_x nanowires.[11] The vapor-solid mechanism occurs when chemical species in the flame diffuse toward the tungsten wire and adsorb onto the substrate to form nanowires.[17] The probed position in the methane flame is characterized by large and comparable amounts of O_2, H_2O, and CO_2 (at +0.88 cm from the bottom burner). At these elevated temperatures, the tungsten oxide nanostructures observed may be formed thorough reactions with any of these species. As seen in Table 4.1, H_2O is by far the most dominant species present at the probed location, suggesting that a hydrothermal route is most likely in forming the larger diameter tungsten oxide nanowires in the hydrogen flame. The Gibbs free energies[24] of possible reactions can be calculated to gain insight into growth mechanisms. One water reaction, both oxygen reactions, and both carbon dioxide reactions have negative values, meaning

they are possible routes to form WO_3. The water vapor and oxygen routes are possible followed by a hydrogen reduction based on the Gibbs free energy values calculated below. Although the Gibbs free energy for Eq. 4.3 is positive, indicating that the reaction does not proceed in the direction given, WO_3 in the solid phase can be formed by carbon dioxide and can provide the initial seeds for nanowires growth through the water vapor and oxygen route.

$$W^{(s)} + 1.5O_2{}^{(g)} \rightarrow WO_3{}^{(g)} \qquad \Delta G_{1800\,K} = -192.8 \qquad (4.1)$$

$$WO_3{}^{(g)} + 0.1\ H_2{}^{(g)} \rightarrow WO_{2.9}{}^{(s)} + 0.1\ H_2O^{(g)} \qquad \Delta G_{1800\,K} = -208.2 \qquad (4.2)$$

$$W^{(s)} + 3\ CO_2{}^{(g)} \rightarrow WO_3{}^{(g)} + 3\ CO^{(g)} \qquad \Delta G_{1800\,K} = +188.3 \qquad (4.3)$$

$$WO_3{}^{(g)} + 0.1\ H_2{}^{(g)} \rightarrow WO_{2.9}{}^{(s)} + 0.1\ H_2O^{(g)} \qquad \Delta G_{1800\,K} = -208.2 \qquad (4.4)$$

$$W^{(s)} + 2\ H_2O^{(g)} \rightarrow WO_2(OH)_2{}^{(g)} + H_2{}^{(g)} \qquad \Delta G_{1800\,K} = -223.4 \qquad (4.5)$$

$$WO_2(OH)_2{}^{(g)} + 0.1\ H_2{}^{(g)} \rightarrow WO_{2.9}{}^{(s)} + 1.1\ H_2O^{(g)} \qquad \Delta G_{1800\,K} = -30.2 \qquad (4.6)$$

$$W^{(s)} + 3H_2O^{(g)} \rightarrow WO_3{}^{(s)} + 3H_2{}^{(g)} \qquad \Delta G_{1800\,K} = -545.7 \qquad (4.7)$$

$$W^{(g)} + 3H_2O^{(g)} \rightarrow WO_3{}^{(s)} + 3H_2{}^{(g)} \qquad \Delta G_{1800\,K} = +43.7 \qquad (4.8)$$

$$2W^{(s)} + 3O_2{}^{(g)} \rightarrow 2WO_3{}^{(s)} \qquad \Delta G_{1800\,K} = -796.7 \qquad (4.9)$$

$$2W^{(g)} + 3O_2{}^{(g)} \rightarrow 2WO_3{}^{(s)} \qquad \Delta G_{1800\,K} = -1975.3 \qquad (4.10)$$

$$2W^{(s)} + 3CO_2{}^{(g)} \rightarrow 2WO_3{}^{(s)} + 2CO^{(g)} \qquad \Delta G_{1800\,K} = -146.4 \qquad (4.11)$$

$$2W^{(g)} + 3CO_2{}^{(g)} \rightarrow 2WO_3{}^{(s)} + 2CO^{(g)} \qquad \Delta G_{1800\,K} = -735.7 \qquad (4.12)$$

Air Side		
Species	CH_4 (mol/m^3)	H_2 (mol/m^3)
O_2	11.83	2.54
H_2O	13.39	16.20
CO	0.77	0.00
OH	0.39	3.48
CO_2	14.65	0.00

Table 4.1 Concentrations of species in the methane and hydrogen flame on the air side.

4.3.2 Fuel-Side

To further assess non-oxygen reaction routes toward the formation of these nanostructures, the experiment is conducted probing a location with the same temperature on the fuel side of the reaction zone, which has different species concentrations (see Figure 4.1). Interestingly, the nanowires formed on the fuel side (with no oxygen present) are thinner and longer than those obtained by probing the air side. In Figure 4.6 (a) and (b) the tungsten oxide nanowires grown on the fuel side of the methane flame are less than 50 nm in diameter and more than 2 μm in length. In Figure 4.7 (a) and (b), the nanowires grown in the hydrogen flame are less than 150 nm in diameter and greater than 5 μm long.

(a) 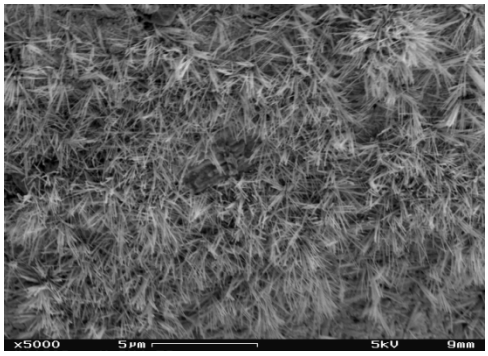 (b) 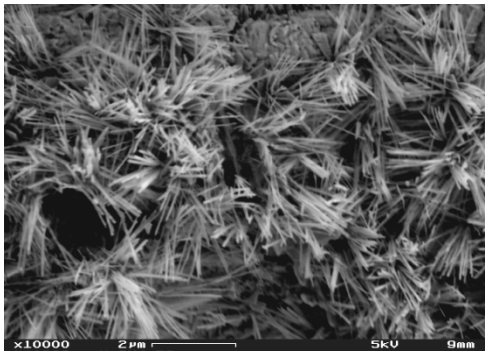

Figure 4.6 (a) Low magnification tungsten oxide nanowires grown on the fuel side of a CH_4 CDF (b) Magnified image of nanowires grown in CH_4

(c) 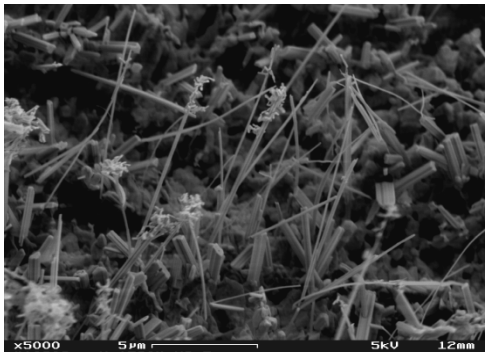 (d) 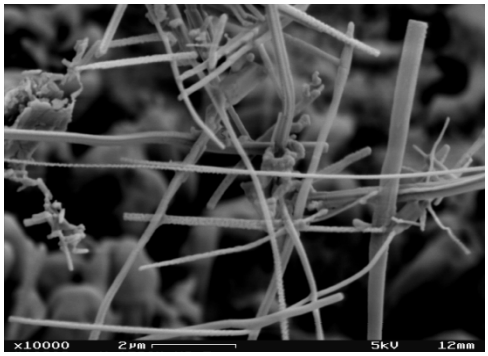

Figure 4.7 (a) Low magnification showing tungsten oxide from H_2 flame (b) Typical image of tungsten oxide grown on the fuel side of the H_2 flame

An image of tetragonal $WO_{2.9}$ nanowires grown on the fuel side in the methane flame are shown in Figure 4.8(a), but the growth direction is in the [2,0,0] direction as opposed to the [1,1,0] direction seen before on the air side. Figure 4.8(b) and (c) show $WO_{2.9}$ grown on the fuel side of the hydrogen flame. The growth direction has again changed and is in the [1,0,1] direction.

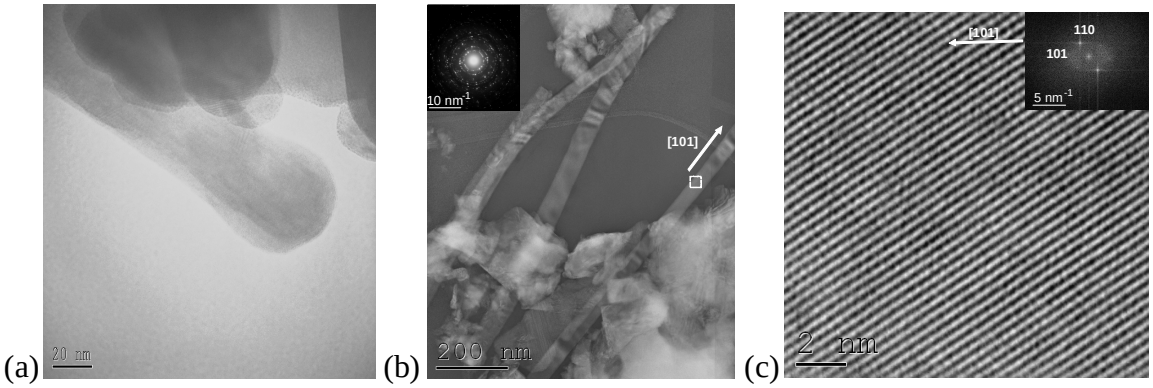

Figure 4.8 (a) TEM image of nanowires grown on the fuel side of the methane flame (b) TEM image of tungsten oxide nanowires grown on the fuel side of the hydrogen flame with an inset of the diffraction pattern (c) High resolution TEM image along with FFT analysis in the upper right corner

In the methane flame there are sufficient concentrations of H_2O and CO_2 to form tungsten oxide. Since there is no carbon in the hydrogen flame structure, H_2O is the only species present in high enough levels to be able to form tungsten oxide. The similarity of the structures of Figure 4.4(b) and Figure 4.7(b) suggest that the tungsten oxide made in the hydrogen flame is being formed through a water route. It seems as though the water route produces larger diameter nanowires than a CO_2 route.

Interestingly, WC_x is not formed in our system. In looking at the Gibbs free energies[24] of the reactions in Eqns. 4.13-4.15 it can be seen that they are spontaneous, so it is likely that the kinetic reaction rates play a key role. The activation energy, which controls the kinetic rates, is probably much larger for the tungsten carbide reactions. This may be a contributing factor as to why tungsten oxide is the preferred growth structure. In other works tungsten carbide was only formed when the substrate temperatures were above 1673 K, which is much higher than the temperatures found in our experiments.[25,26,27,28]

$$W^{(g)} + CH_4{}^{(g)} \rightarrow WC^{(g)} + 2H_2{}^{(g)} \qquad \Delta G_{1800\,K} = -731 \qquad (4.13)$$

$$W^{(g)} + C^{(g)} \rightarrow WC^{(g)} \qquad \Delta G_{1800\,K} = -1057 \qquad (4.14)$$

$$W^{(s)} + C^{(g)} \rightarrow WC^{(s)} \qquad \Delta G_{1800\,K} = -468 \qquad (4.15)$$

Fuel Side		
Species	CH_4 (mol/m^3)	H_2 (mol/m^3)
O_2	0.41	0.05
H_2O	15.05	19.89
CO	5.22	0.00
OH	0.00	0.90
CO_2	15.56	0.00

Table 4.2 Species concentrations in methane and hydrogen flame structure on the fuel side.

4.4 Conclusions

In summary, we performed a parametric study to correlate local growth conditions with morphologies. In the methane flame, H_2O and CO_2 play a role in growth conditions, but in the hydrogen flame only H_2O is present in the flame proving that is a growth mechanism to form tungsten oxide nanowires. In the methane flame, aligned nanowires approximately 50 nm in diameter were grown on the air side, while thinner (<50 nm) wires were found on the fuel side. The hydrogen flame the nanowires were not aligned and were about 200 nm in diameter on the air side. The fuel side of the hydrogen flame produced nanowires that were ~150 nm in diameter. The growth direction of the nanowires varied for each case. Also, the effect of electric fields on the morphology was investigated, where instead of nanowires, saw and comb shapes were obtained.

Chapter 5

Zinc Oxide Nanostructures

5.1 Introduction

Many zinc oxide nanostructures have been developed in recent years, such as nanowires, nanorods, nanobelts, nanoneedles, nanosprings, nanorings, nanobows, and nanohelices.[29, 30] Its non-central symmetric wurzite lattice structure, along with electromechanical coupling, enhances piezoelectric and pyroelectric properties.[31] Zinc oxide also has a wide band gap (3.37 eV), which makes it a good semiconductor material. These unique characteristics can be utilized in actuators, piezoelectric sensor, nanogenerators, biosensor, and biodetectors.[32, 33] There are many methods for the fabrication of these nanomaterials, such as vapor-liquid-solid growth, solution-liquid-solid methods, template mediate growth, electron beam lithography, scanning tunneling microscopy techniques, and many more based on the desired morphologies and properties. Many of these methods are complex and give little or no insight into the different types of ZnO growth mechanisms.

Zinc can be oxidized by interactions with water vapor, carbon dioxide, and oxygen, all of which are present in a methane diffusion flame. In this work ZnO nanostructures are synthesized in methane and hydrogen diffusion flames to isolate growth mechanisms and perform a parametric study of local growth conditions. We explore zinc substrate interactions with H_2O, CO_2, and O_2. A zinc-plated steel probe is inserted into a counterflow diffusion flame (CDF) at various axial distances in order to correlate morphologies with local growth conditions.

5.2 Experiment

CDFs with either nitrogen-diluted methane or nitrogen-diluted hydrogen as fuel are used to study the flame synthesis of ZnO nanowires. Again, the temperature profiles of the methane and hydrogen flames have been strategically matched in order to compare chemical species while keeping temperature constant. H_2O, CO_2, and O_2 are present in the methane flame and can cause variations in the morphology of the ZnO nanostructures.[29] To distinguish the roles, a hydrogen flame is utilized because only H_2O and O_2 are present. Below are the graphs of the temperature and species concentrations of the two flame structures computed using GRI-Mech 1.2.[4]

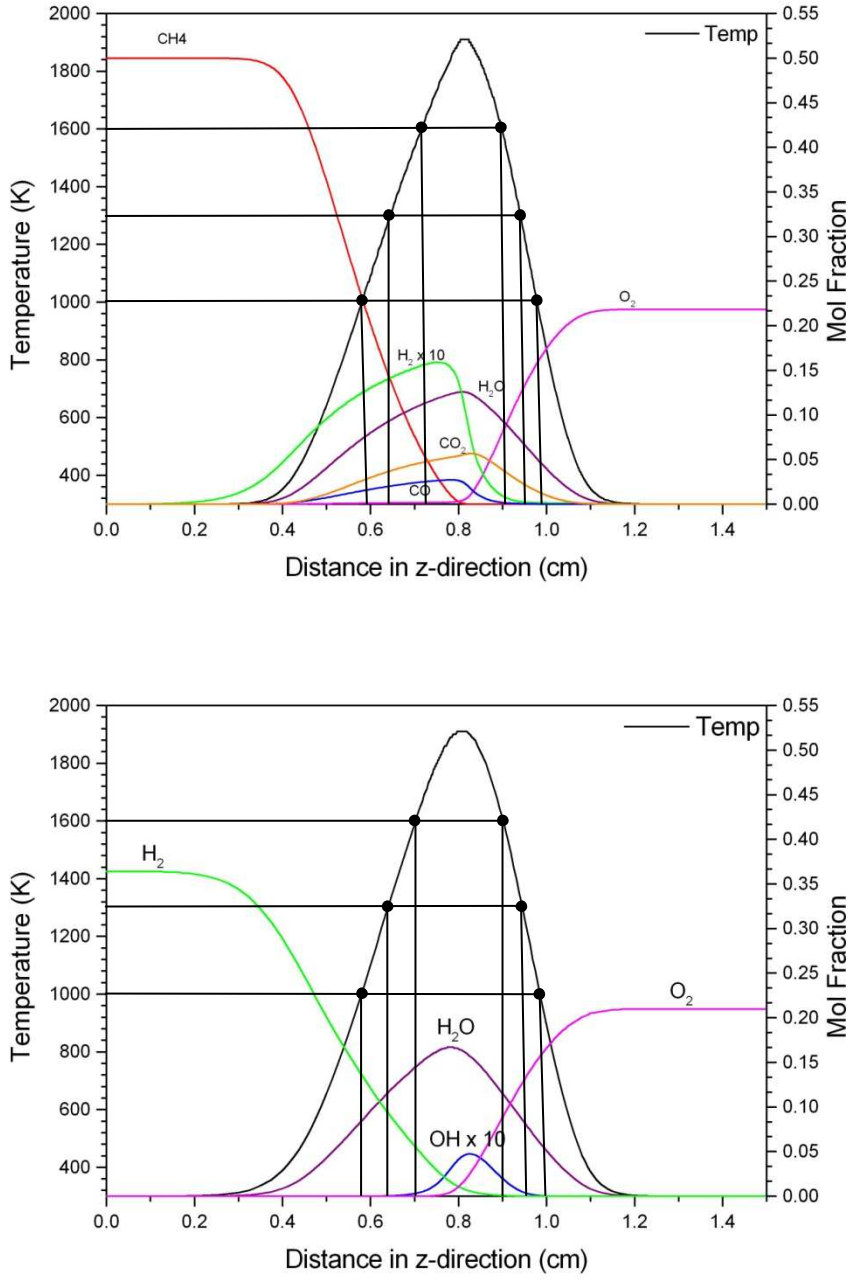

Figure 5.1 Gas phase flame structure of methane flame with 50% CH_4 and 50% N_2 (top) and hydrogen flame with 36.5% H_2 and 63.5% N_2 (bottom).

A zinc substrate probe is inserted into a CDF at a position on either the air or the fuel side of the flame in ambient conditions where the temperature is 1000 K, 1300 K, or 1600 K for 10 minutes. The morphologies of as-grown nanostructures are examined using field emission scanning electron microscopy (FESEM, LEO Zeiss Gemini 982). Structural features of the nanomaterials are investigated using high resolution transmission electron microscopy (HRTEM, TOPCON 002B), along with selected area electron diffraction (SAED).

5.3 Results

5.3.1 Air Side

All of the positions probed on the air side of both methane and hydrogen flames produced nanostructures. Below, in Figures 5.2 and 5.3 are images of the nanomaterials formed in methane and hydrogen diffusion flames at 1600 K (z=9 mm). Due to the vapor-liquid-solid growth mechanism, many different structures can form from zinc droplets, but most of the structures range from 300 – 500 nm in diameter and have symmetrical hexagonal facets. Figure 5.2(a) shows hexagonal nanorods with diameters of approximately 450 nm. Nanorods with "welded" joints and sharp tips can be seen in Figure 5.2(b) and (c).[34,35] Figure 5.2(d) and (e) show gradually decreasing cross-sections from top to bottom, which are can be described as "nanonails" and flower-like patterns.[36,37] The last two images are complicated structures developed by multiple growth directions of nanorods. In Figure 5.2(g) the nanostructures are called tetrapod-shaped structures and have a hexagonal cross section with uniform diameter.[38,39]

Nanorods composed of smaller more complex nanostructures can be seen in Figure 5.3(a). An area of nanoribbons less than 500 nm wide is shown in Figure 5.3(b). In Figure 5.3(c), longer nanorods with sharp tips are produced from the hydrogen flame. The image in Figure 5.3(d) is similar to the complex nanostructures seen in Figure 5.2(f).

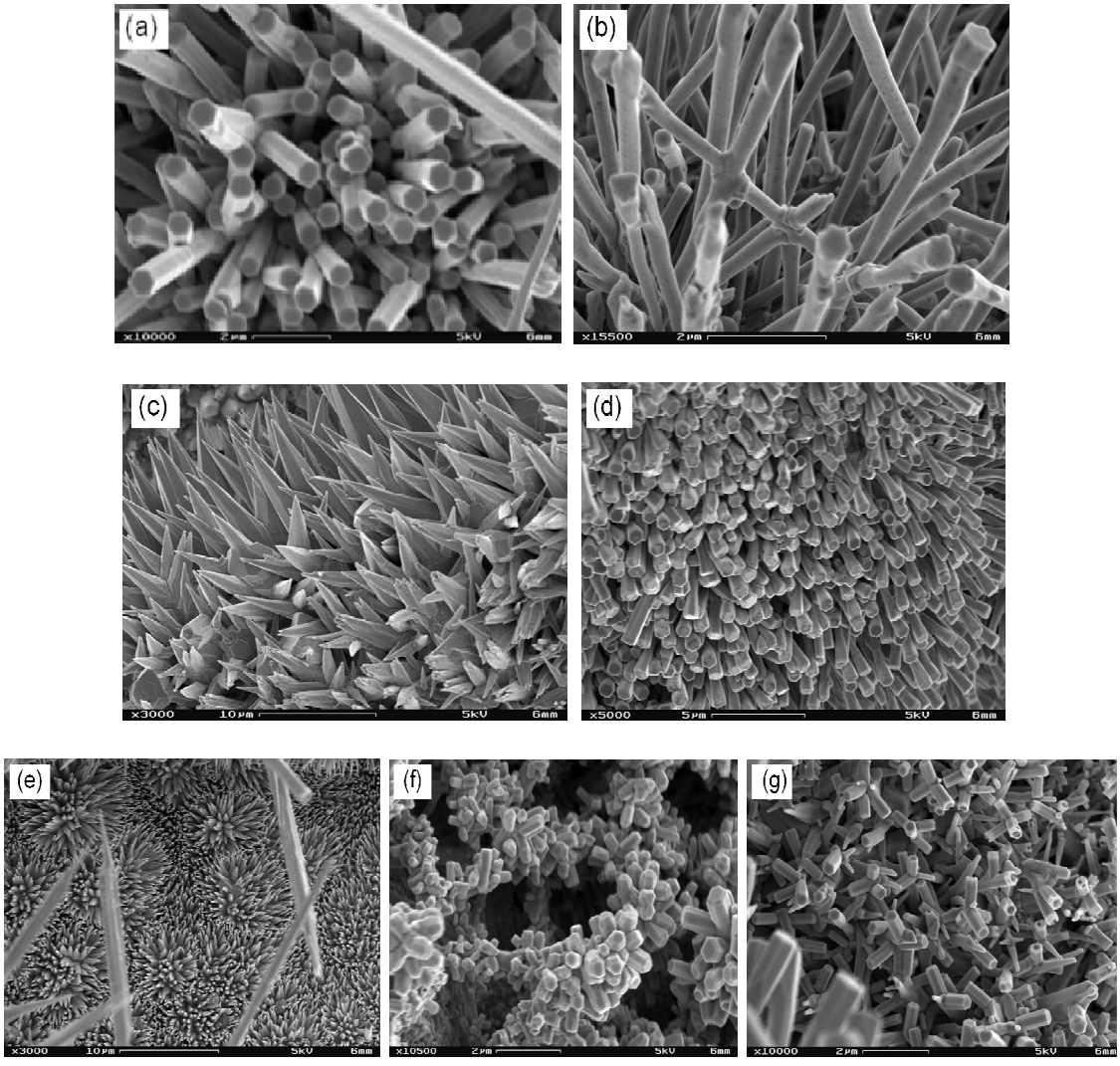

Figure 5.2 FESEM images of nanomaterials from the CH_4 flame on the oxidizer side where T = ~1600K and z=+0.90cm.

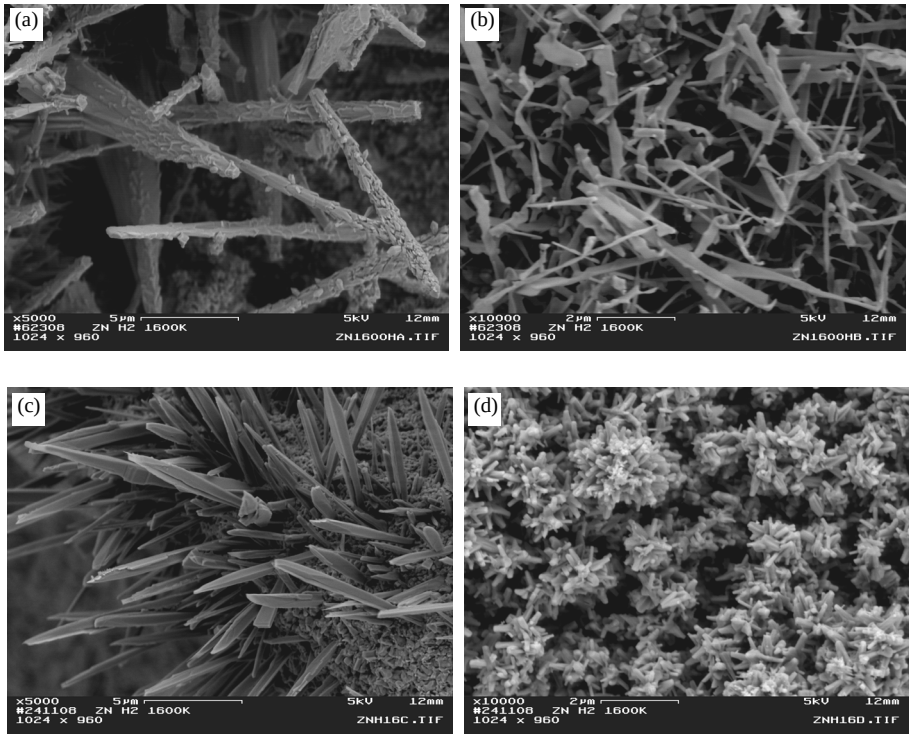

Figure 5.3 FESEM images of nanomaterials from the H_2 flame on the oxidizer side where T=~1600K and z=+0.90cm.

Images of the nanomaterials obtained from the oxidizer side where the temperature is 1300 K (*z*=9.4 mm) can be seen in Figure 5.4 and Figure 5.5. The nanorods in Figure 5.4(a) display hexagonal facets. Figure 5.4(b) shows nanoribbons approximately 50 nm wide intermixed with smaller diameter nanowires that are about 20 nm. Tower-like structures are observed in Figure 5.4(c) and are stacked layer upon layer.[43] Also, Figure 5.4(d) is composed of many ZnO sharp cones connected to one another forming chain-like structures.

Images of large nanorods a few hundred nanometers in diameter are seen in Figure 5.5 (a). Nanostructures similar to the tetrapod-shaped structures, which have arms extending from the center of the structure, are evident in Figure 5.5(b).

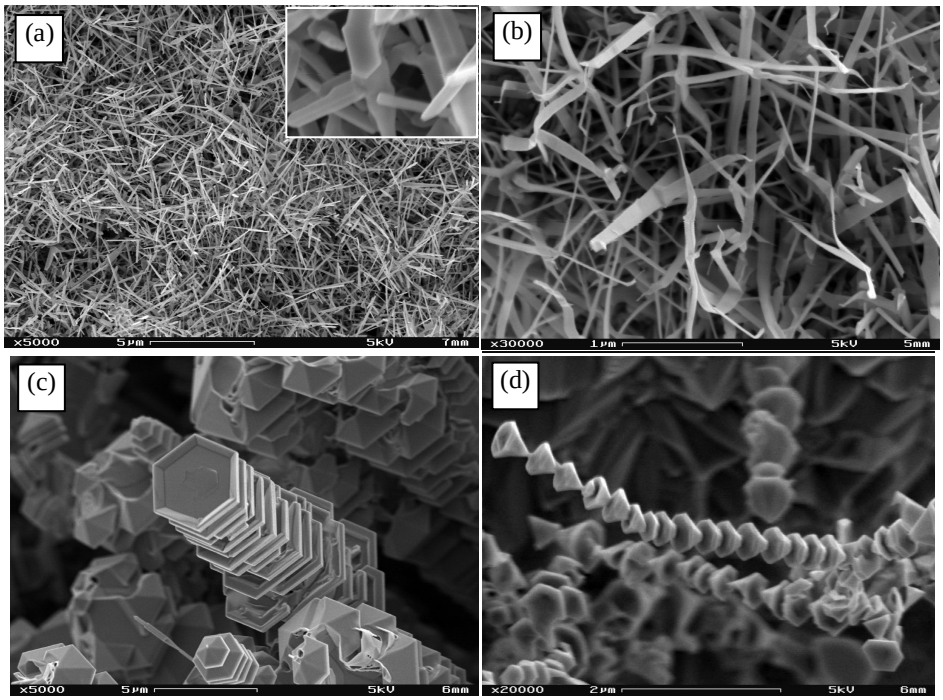

Figure 5.4 FESEM images of nanomaterials from the CH_4 flame on the oxidizer side where T = ~1300K and z=+0.94cm: (a) nanorods, (b) nanoribbons, (c) tower-like structure, (d) chain-like structure.

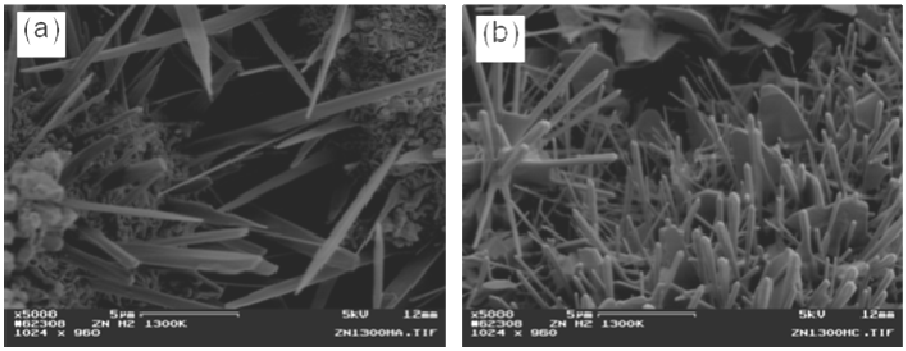

Figure 5.5 FESEM images of nanomaterials from the H_2 flame on the oxidizer side where T=~1300K and z=+0.94cm.

The final position probed is at 1000 K, and the main structures formed from the methane flame are micro-sized columns as seen in Figure 5.6(a). They are most likely seeded from large size zinc droplets on the substrate surface. Figure 5.6(b) shows nanosheets

with a thickness of about 50 nm, and various shapes are seen radially away from the centerline. The hydrogen flame produces large diameter nanorods approximately 300 nm in diameter.

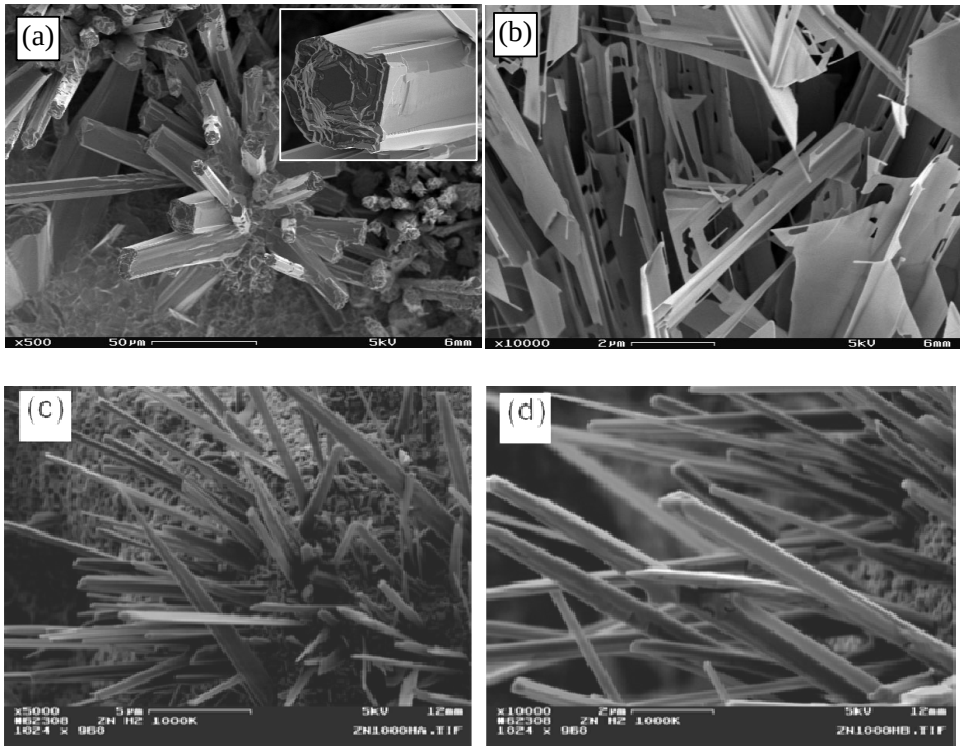

Figure 5.6 FESEM images of nanomaterials from the axial position on the oxidizer side where T = ~1000K and z=+0.98cm: (a) microsized columns/chunks (CH_4), (b) nanosheets (CH_4), (c) and (d) nanorods from the H_2 flame.

The chart below shows the concentrations of the relevant species for ZnO growth. The methane flame supplies carbon, oxygen, and hydrogen, while the hydrogen flame lacks any carbon containing compounds. Therefore, a parametric study can be performed to narrow down the growth mechanisms for ZnO. The methane flame at 1000 K and 1300 K have significantly more O_2 than any other species present; but at 1600 K, O_2, H_2O, and CO_2 are similar in amounts to each other. Therefore, at 1600 K, there are more routes available to grow the nanomaterials, and more morphologies may be present as shown

previously. At 1300 K, there are still more morphologies present than at 1000 K, where the oxygen concentration is almost seven times higher than any other species in the flame.

In the hydrogen flame there is no CO or CO_2 present in the flame. Therefore, only O_2 and H_2O can be growth mechanisms for the ZnO formation. Again, at 1000 K the O_2 concentration is much higher than H_2O, and the H_2O concentration increases while the O_2 concentration decreases as the temperature is increased. At 1600 K various nanostructures can be grown with ease. Then at 1300 K there are less morphologies that are able to be grown, and finally at 1000 K only large diameter nanorods can be produced.

Air Side						
Species	CH_4 1000K (mol/m^3)	CH_4 1300K (mol/m^3)	CH_4 1600K (mol/m^3)	H_2 1000K (mol/m^3)	H_2 1300K (mol/m^3)	H_2 1600K (mol/m^3)
O_2	34.23	26.98	17.21	34.91	28.57	20.00
H_2O	6.53	9.14	12.03	7.95	11.02	14.67
CO	0.00	0.12	0.38	0.00	0.00	0.00
OH	0.02	0.07	0.28	0.00	0.06	0.24
CO_2	4.58	7.76	12.22	0.00	0.00	0.00

Table 5.1 Species concentrations for the methane and hydrogen flame on the air side at the probed location.

The reactions that take place in order to form ZnO in solid or gaseous phase involve water vapor, carbon dioxide, and oxygen, and are shown below. The Gibbs free energies[24] of all of the listed reactions are negative, but the sign changes from negative to positive in Eqn. 4 between 1400 and 1600 K. It shows that ZnO formation proceeds favorably up to about 1600 K.

In the reaction of water vapor with liquid zinc, small liquid droplets form, and nanoparticles propagate from these droplets.[40] If the zinc is in the solid phase, the nanostructures can form through an epitaxial process.[40] Zinc vapor can react with water vapor and recondense on the surface of the substrate to form solid ZnO nanomaterials. Oxidation of zinc can also occur with carbon dioxide. The adsorbed zinc can react directly with CO_2, or an autocatalytic effect can take place with CO, which is a byproduct of the Zn and CO_2 reaction.[41] Finally, oxygen can react directly with zinc vapor or droplets to form ZnO.[42]

$$Zn^{(s,l)} + H_2O^{(g)} \rightarrow ZnO^{(s)} + H_2{}^{(g)} \quad (5.1)$$

$$Zn^{(g)} + H_2O^{(g)} \rightarrow ZnO^{(g)} + H_2{}^{(g)} \quad (5.2)$$

$$Zn^{(s,l)} + CO_2{}^{(g)} \rightarrow ZnO^{(s)} + CO^{(g)} \quad (5.3)$$

$$Zn^{(g)} + CO_2{}^{(g)} \rightarrow ZnO^{(g)} + CO^{(g)} \quad (5.4)$$

$$Zn^{(s,l)} + O_2{}^{(g)} \rightarrow ZnO^{(s)} \quad (5.5)$$

$$Zn^{(g)} + O_2{}^{(g)} \rightarrow ZnO^{(g)} \quad (5.6)$$

Gibbs Free Energy (kJ)						
Temp (K)	**5. 1**	**5. 2**	**5. 3**	**5. 4**	**5. 5**	**5. 6**
800	-66.14	-103.93	-56.70	-94.49	-269.73	-307.52
1000	-55.44	-73.07	-52.60	-70.24	-248.15	-265.79
1200	-43.03	-43.03	-46.39	-46.39	-224.61	-224.61
1400	NA	-13.67	NA	-22.91	NA	-183.93
1600	NA	15.11	NA	0.24	NA	-143.72

Table 5.2 Gibbs Free Energy calculations for ZnO formation.[24]

5.3.2 Fuel Side

In order to see the effect of species variations the same temperatures that are probed on the oxidizer side are also probed on the fuel side. On the fuel side of the methane flame at 1600 K, perfect hexagonal nanorods are observed with uniform diameter of ~450 nm, as shown in Figure 5.6(a). These nanorods are almost identical to those shown in Figure 5.2(a), even though the species concentrations are different, i.e. there is a large decrease in O_2 while other species remain the same or increase. As the temperature decreases, the nanowires become narrower. At 1300 K, they have an average diameter of ~150 nm and a length up to 30 µm, as seen in Figure 5.7(b). Probing at 1000 K produces thin nanowires ranging from 30-100 nm in diameter. Away from the flame centerline at this axial position, a very small quantity of nanoribbons can be observed in Figure 5.7(d). These nanoribbons are ~150 nm wide and ~25 nm thick and can be up to several tens of micrometers in length.

In the hydrogen flame at 1600 K, nanorods with sharp tips are the main product yielded, which are shown in Figure 5.8(a). Complex nanostructures are present at the axial positions where the temperatures are 1000 K and 1300 K, as can be seen in Figure 5.8(b) and (c). No nanorod or nanowires are found on the air side of the hydrogen flame.

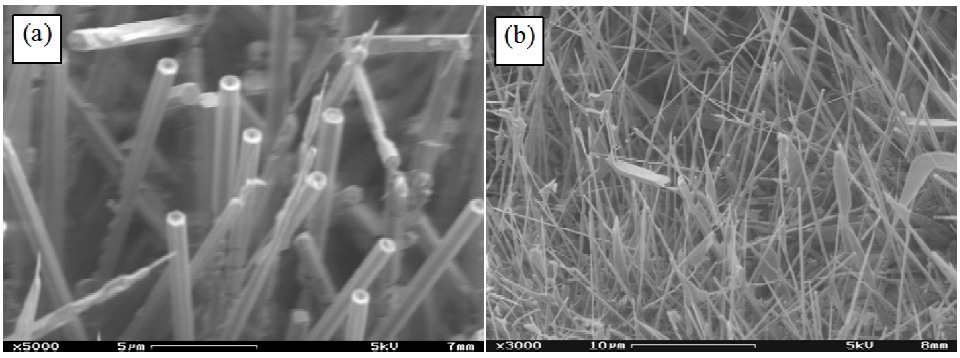

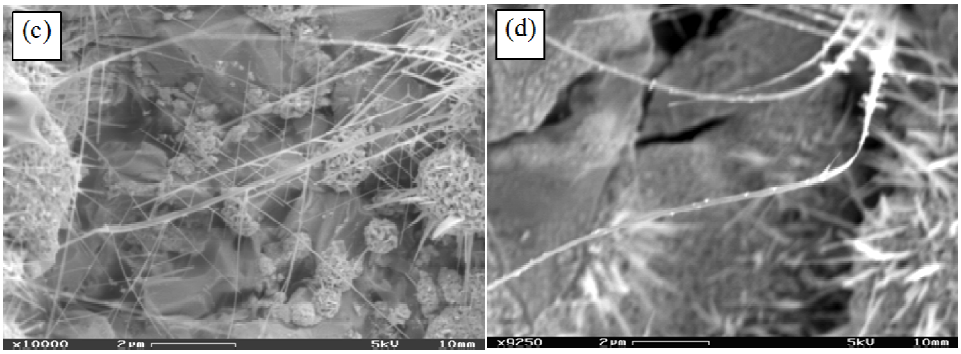

Figure 5.7 ZnO nanomaterials from the fuel side of the methane flame. (a) T = ~1600 K, (b) T = ~1300 K, (c) and (d) T = ~1000 K.

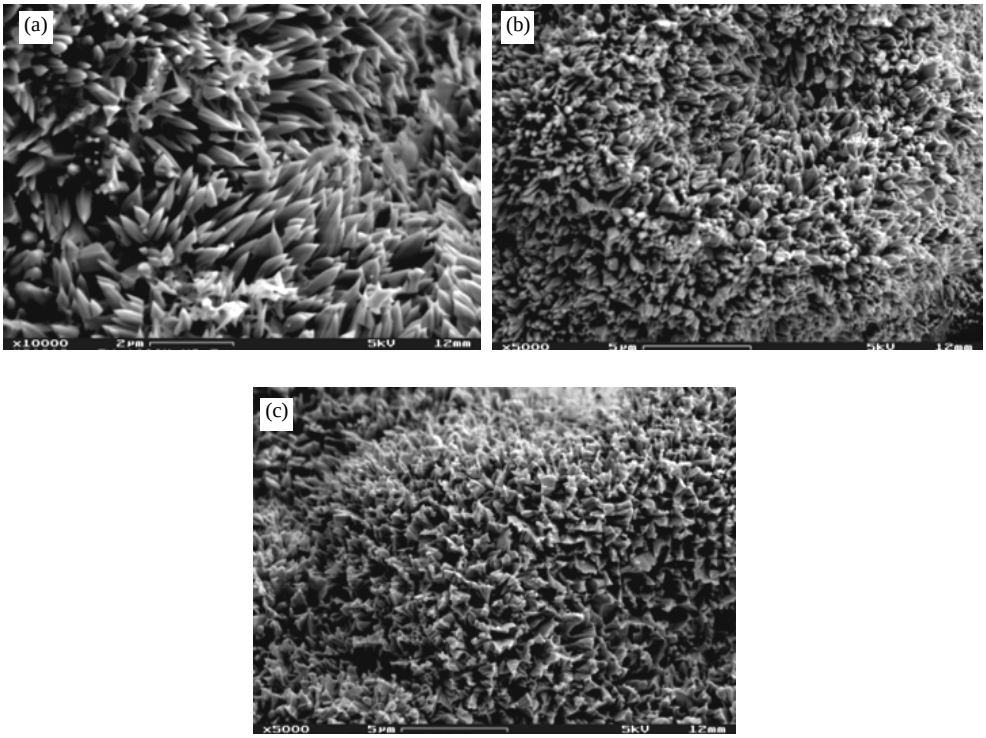

Figure 5.8 ZnO nanomaterials grown in the hydrogen flame at (a) 1600 K, (b) 1300 K, and (c) 1000 K.

In the methane flame on the fuel side there is very little O_2 present, but H_2O, CO, and CO_2 are the main species components in the area between 1000 and 1600 K. Hu *et al.*[39] concluded that ZnO morphologies are closely related with the reaction temperature, oxygen partial pressure, and flow rate. Wang *et al.*[43] reported that temperature, vapor

flow, and availability of Zn and O vapor affect the morphologies of as-prepared ZnO structures. Gao *et al.*[44] also mentioned that local temperature and surface diffusion rate have an influence on ZnO nanostructures. Nevertheless, in general, the ZnO nanomaterials produced in CDFs are quite uniform (even in the radial direction), namely, one structure or morphology constitutes the major product (~70% by volume) of harvested material at a given axial position. The sensitivity of ZnO nanostructures to a slight radial gradient is likely due to a liquid Zn layer on the surface of the probe, which is susceptible to the Marangoni effect. A liquid layer of zinc exists on the substrate surface due to its low melting point (692K). The surface tension of this liquid layer is temperature dependent and would decrease with increasing temperature.[45] Thus a surface tension gradient is created on the liquid layer resulting from the presence of a temperature gradient along the radial direction of the substrate. Such a gradient in surface tension causes liquid to flow away from regions of low surface tension to those of high surface tension, which pull more strongly on the surrounding liquid. This mechanism intermixes adjacent regions, likely affecting the local nucleation of ZnO nanostructures, the preferential faceting of nanostructures, the local reaction of Zn with H_2O, and the absorption of ZnO vapor, resulting in the different nanostructures and morphologies of final as-grown ZnO, along the radial length of the probe.

In the hydrogen flame, the only species present on the fuel side is H_2O. Therefore, any nanostructures grown on the fuel side are synthesized through the H_2O route. The ZnO nanostructures grown from the methane flame tend to have smaller diameters than those grown in the hydrogen flame. This may be due to the CO and CO_2 present in the

methane flame. Larger materials tend to be produced through a purely H_2O route than when other oxygen containing species are present.

Fuel Side						
Species	CH_4 1000K (mol/m3)	CH_4 1300K (mol/m3)	CH_4 1600K (mol/m3)	H_2 1000K (mol/m3)	H_2 1300K (mol/m3)	H_2 1600K (mol/m3)
O_2	0.23	3.17	3.85	0.00	0.00	0.00
H_2O	9.30	12.03	14.16	11.31	14.67	18.36
CO	2.96	4.03	4.88	0.00	0.00	0.00
OH	0.00	0.00	0.00	0.00	0.00	0.02
CO_2	8.17	11.69	14.46	0.00	0.00	0.00

Table 5. 3. Species concentrations for the methane and hydrogen flame on the fuel side at the probed location.

5.4 Conclusions

In summary, we have demonstrated the ability to grow ZnO nanostructures at 1000, 1300, and 1600 K. We have also performed a parametric study to isolate local conditions determining the growth mechanisms at play when synthesizing ZnO nanostructures. There appears to be a vapor-liquid-solid growth mechanism, with key parameters being radical species present, oxidizer, carbon dioxide, and water vapor concentrations, substrate temperature, and gas-phase temperature.

Chapter 6

Molybdenum Oxide Nanoplates

6.1 Introduction

Molybdenum oxide has been studied in recent years due its very valuable catalytic, optical, mechanical, and electronic properties. Molybdenum oxide can be applied for use in sensors, petroleum refining, recording media, and chemical synthesis.[46,47,48] Various techniques for molybdenum oxide synthesis have been reported in the literature, such as high-temperature low-pressure synthesis, chemical reaction, infrared irradiation, and flame synthesis processes. Zhou *et al.*[48,49] has synthesized MoO_2 and MoO_3 nanowires in high temperature and low pressure environments. Niederberger *et al.*[50] utilized a hydrothermal process to form $\alpha MoO_3 \cdot H_2O$, which was washed and dried in order to produce nanofibers. Dhas *et al.*[51] used a sonochemical process to synthesize Mo_2O_5, which relies on high temperatures and pressures created by the cavitation of bubbles. Li *et al.*[52] produced MoO_3 nanobelts and nanotubes through an infrared irradiation process. Suemitsu *et al.*[53] formed MoO_2 hollow fibers by heating a molybdenum substrate in an oxygen/acetylene flame to ~1150°C for 90 minutes. Merchan-Merchan *et al.*[54] produced molybdenum oxide whiskers by heating a substrate in a methane/acetylene counterflow diffusion flame for 2 minutes.

In this work, MoO_2 nanoplates are formed by flame synthesis in methane and hydrogen counterflow diffusion flames (CDF). A parametric study is performed to better assess the growth routes involved in the formation of the unique nanostructures. Molybdenum can

be oxidized with oxygen, water vapor, and carbon dioxide to form molybdenum oxide nanomaterials.[55,56,57]

6.2 Experiment

A CDF with methane or hydrogen diluted with nitrogen as fuel is used to perform the experiments. The CDF is utilized due to its quasi one-dimensional flame structure, along with its amenability to allow chemical species to be tailored according to certain specifications. The temperature profiles of the methane and hydrogen flames are strategically matched in order to compare chemical species. Below are graphs of the temperature and species concentrations of the two flame structures utilized, as obtained by computational simulations using GRI-Mech 1.2.[4]

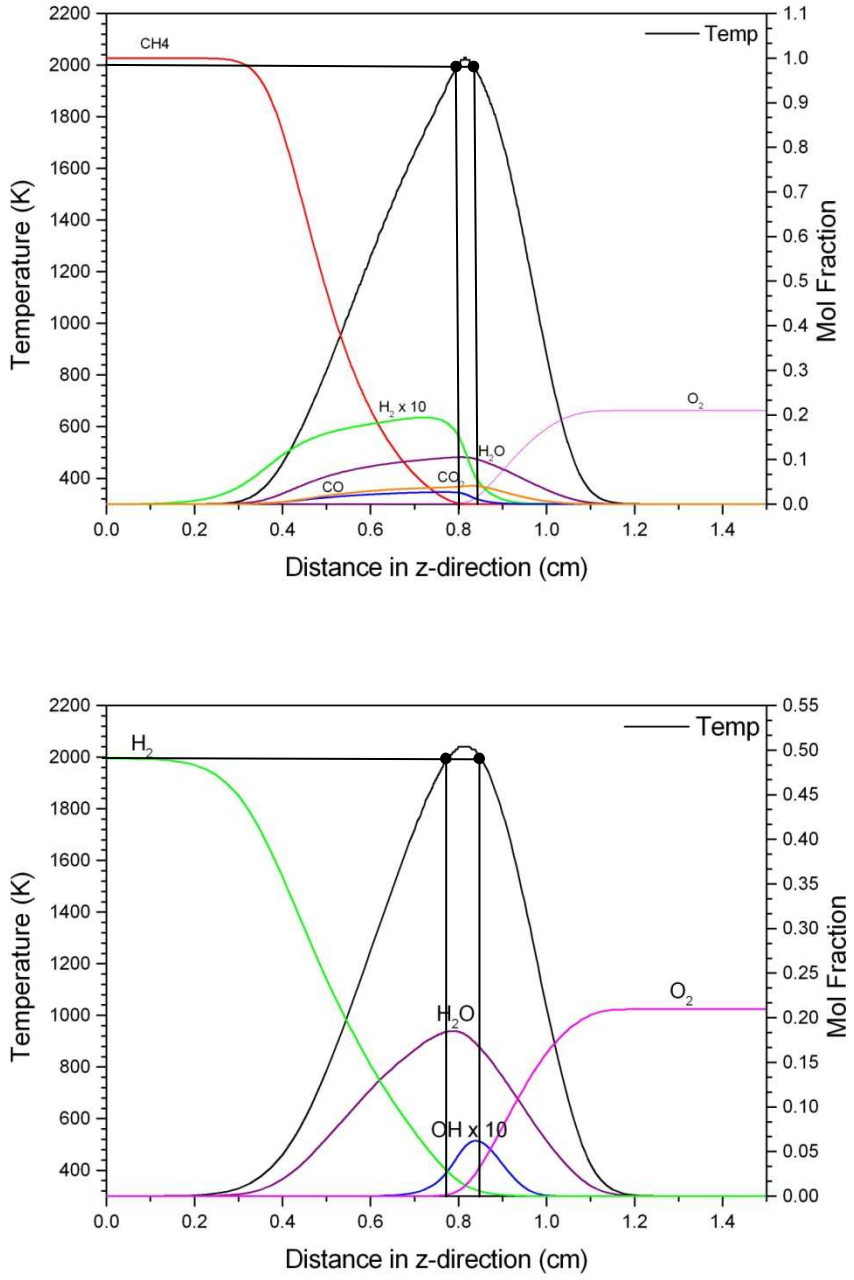

Figure 6.1 Gas phase flame structure of methane flame with 100.0% CH_4 (top) and hydrogen flame with 44.0% H_2 and 56.0% N_2 (bottom).

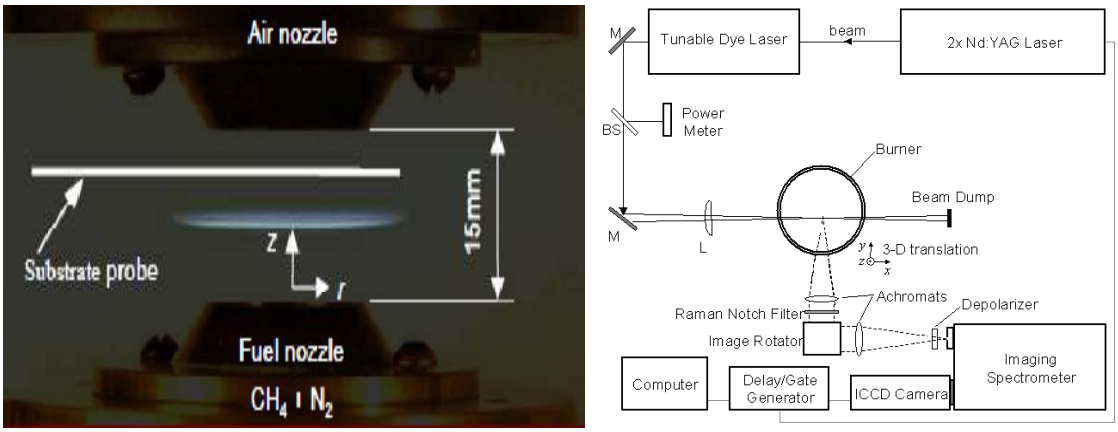

Figure 6.2 (a) Counterflow diffusion flame with probed positions marked. (b) SRS diagnostic setup.

A molybdenum substrate, which is sonicated in methanol to remove contaminants on the surface of the substrate, is inserted into a CDF at a position on either the air side or the fuel side of the flame at atmospheric pressure. The flame temperature is ~2000K at the probed location, and the sample time is 10 minutes. Using an optical pyrometer, the temperature of the substrate is measured to be ~1500K. The morphologies of as-grown nanostructures are examined using field emission scanning electron microscopy (FESEM, LEO Zeiss Gemini 982). Structural features of the nanomaterials are investigated using high resolution transmission electron microscopy (HRTEM, TOPCON 002B), along with selected area electron diffraction (SAED).

6.3 Results

6.3.1 Air Side

Various molybdenum oxide structures are grown at all of the probed locations in the flame. On the air side of the methane flame, molybdenum-oxide nanoplates are formed; and on the air side of the hydrogen flame, molybdenum oxide nanostructures are

synthesized. The nanoplates, shown in Figure 6.3(a) and (b), are a few hundred nanometers wide, about 50 nm thick, and about one micron in length. The nanostructures, which are shown in Figure 6.3(c) and (d), are bundles that seem to grow directly from the substrate surface by oxidation of the metal.

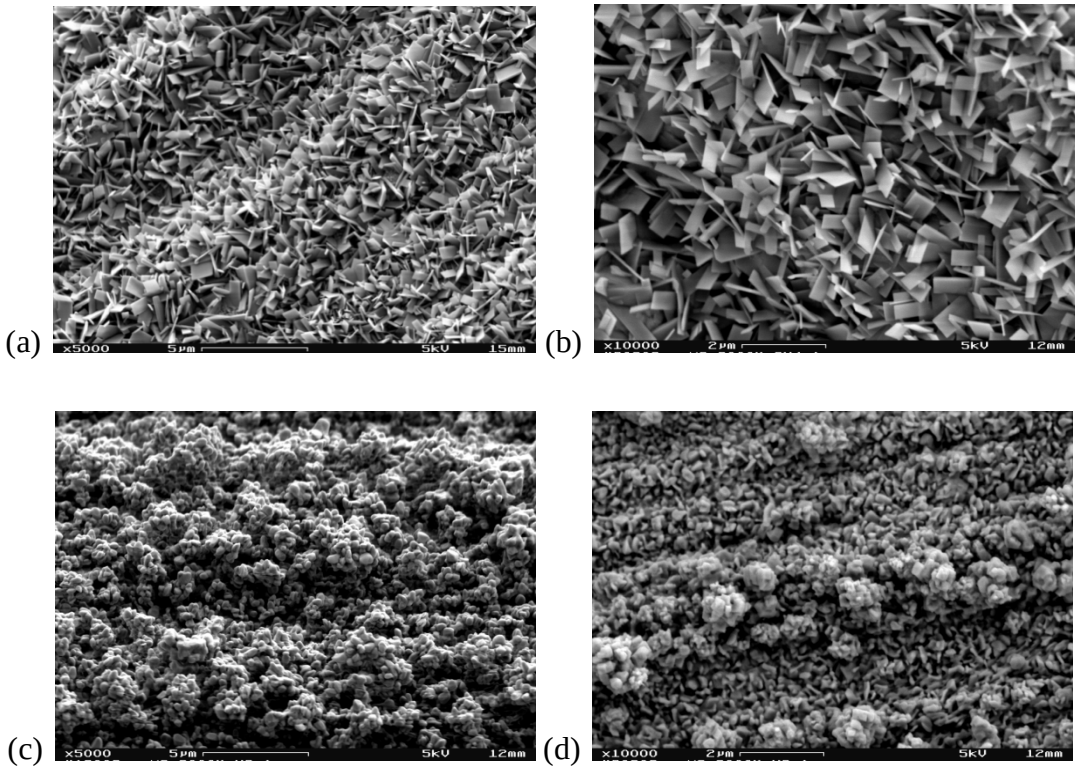

Figure 6.3 Molybdenum oxide grown in the CH_4 flame on the air side (z=+.83cm) at (a) low magnification (b) and high magnification. Molybdenum oxide grown in the H_2 flame on the air side (z=+.83cm) at (c) 5,000X (d) and 10,000X.

On the oxidizer side of the flame the molecular structure is confirmed to be MoO_2 by using SAED, which can be seen as an inset in Figure 6.4. Figure 6.4 shows a nanoplate approximately 100 nm wide with [-1,0,2] growth direction.

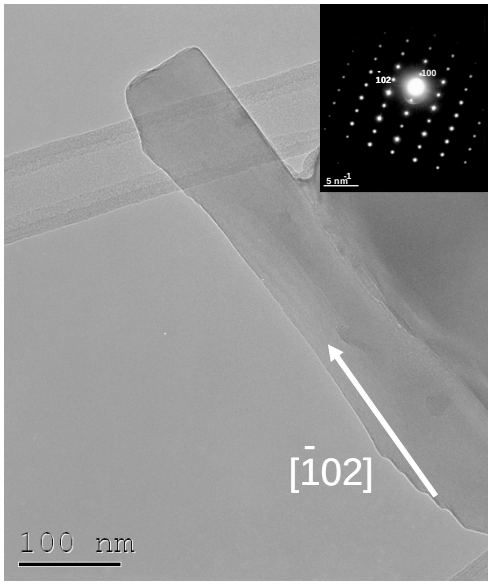

Figure 6.4 TEM image of molybdenum oxide grown in the CH_4 flame on the air side with a diffraction pattern inset.

The concentrations of the gaseous species within the methane and hydrogen flames on the air side are shown in Table 6.1. There are comparable amounts of water vapor and carbon dioxide in the methane flame at +0.83 cm, but the oxygen concentration is very low. Therefore, nanoplates are being formed by either a water vapor or carbon dioxide route. Based on the structures of the MoO_2, a vapor-solid mechanism seems to be at play for the nanoplates grown in the methane flame. Although 2000 K is much less than the melting point of molybdenum, which is 2890 K, some particles may vaporize and react with oxygen in the air to form molybdenum oxide. The reactions below all have negative Gibbs free energies,[24] except Eq. 6.3, which means that all but one of these growth routes are spontaneous. Looking at the species concentrations in the hydrogen flame, there are no carbon containing species present, and the water vapor concentration is three times larger than the oxygen concentration. Based on the nanostructure growth, it is inferred

that surface oxidation is occurring on the surface of the substrate. Therefore, Eqn. 6.1 gives the most probable reaction mechanism.

$$Mo^{(s)} + O_2^{(g)} \rightarrow MoO_2^{(s)} \qquad \Delta G_{2000K} = -241.3 \qquad (6.1)$$

$$Mo^{(g)} + O_2^{(g)} \rightarrow MoO_2^{(g)} \qquad \Delta G_{2000K} = -442.5 \qquad (6.2)$$

$$Mo^{(s)} + 2H_2O^{(g)} \rightarrow MoO_2^{(s)} + 2H_2^{(g)} \qquad \Delta G_{2000K} = +30.3 \qquad (6.3)$$

$$Mo^{(g)} + 2H_2O^{(g)} \rightarrow MoO_2^{(g)} + 2H_2^{(g)} \qquad \Delta G_{2000K} = -170.9 \qquad (6.4)$$

$$Mo^{(s)} + 2CO_2^{(g)} \rightarrow MoO_2^{(s)} + 2CO^{(g)} \qquad \Delta G_{2000K} = -20.9 \qquad (6.5)$$

$$Mo^{(g)} + 2CO_2^{(g)} \rightarrow MoO_2^{(g)} + 2CO^{(g)} \qquad \Delta G_{2000K} = -222.1 \qquad (6.6)$$

Air Side		
Species	CH_4 (mol/m^3)	H_2 (mol/m^3)
O_2	1.99	6.98
H_2O	11.33	18.21
CO	2.61	0.00
OH	0.29	0.63
CO_2	11.05	0.00

Table 6.1 Species concentrations in the methane and hydrogen flame on the oxidizer side at 2000K at the probed location (z=+0.83cm).

6.3.2 Fuel Side

On the fuel side of the methane flame, smaller nanoplates are grown than on the air side. In Figure 6.5(a) it can be seen that there is a large coverage density of molybdenum oxide on the substrate surface; and in Figure 6.5(b) it can be seen that the width and length of the nanoplates are less than 100 nm and one micron, respectively. In the hydrogen flame, micron-sized plates are formed. As seen in Figure 6.5(c) and (d) the width and length of

the plates are a few microns, and the thickness is approximately 500 nm. No nanostructures are found on the substrate inserted into the fuel side of the hydrogen flame.

(a) 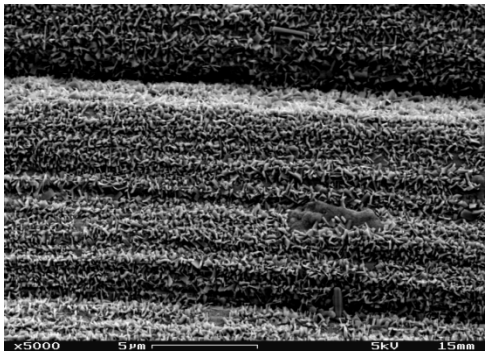

(b) 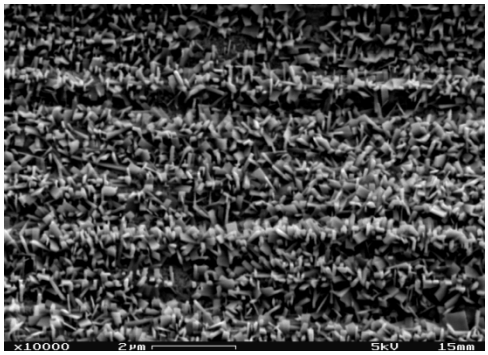

(c) 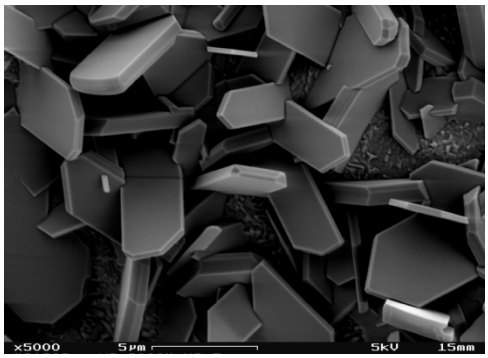

(d) 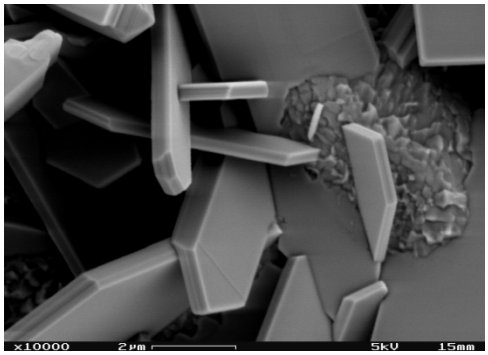

Figure 6.5 Molybdenum oxide grown in the CH_4 flame on the fuel side (z=+0.79cm) at (a) low magnification (b) and high magnification. Molybdenum oxide grown in the H_2 flame on the fuel side at (c) 5,000X (d) and 10,000X.

On the fuel side of the methane and hydrogen flames, there is very little oxygen present. The methane flame has sufficient water vapor and carbon dioxide to form MoO_2 on the fuel side. The hydrogen flame only has water vapor on the fuel side. Therefore, any structures formed in this manner are grown by a water vapor mechanism. Large molybdenum oxide structures are formed through the water vapor route shown in Eqn. 6.4. All of the materials grown on the fuel side appear to be made by a vapor-solid route.

Fuel Side		
Species	CH_4 (mol/m^3)	H_2 (mol/m^3)
O_2	0.41	0.41
H_2O	11.52	20.29
CO	4.44	0.00
OH	0.03	0.31
CO_2	10.46	0.00

Table 6.2 Species concentrations in the methane and hydrogen flame on the fuel side at 2000K at the probed location (z=+0.79).

6.4 Conclusions

Molybdenum oxide nanostructures are formed at 2000 K. In the methane flame on the air side and the fuel side, CO_2 and H_2O are present in large enough concentrations to contribute to nanoplate growth. The hydrogen flame contains water vapor as the largest species concentration. Therefore, on the air side, direct oxidation of the surface occurs; and on the fuel side, micron sized plates are grown through a vapor solid mechanism.

Chapter 7

Copper Oxide and Iron Oxide Nanowires

7.1 Introduction

Various types of metal-oxide nanowires have promising applications due to their unique properties. In particular, copper oxide nanowires can be used to produce optoelectronic, biological, magnetic, and optical devices, as well as catalysts. Cu_2O is a p-type semiconductor, which has a band gap of 2.0 eV. Different methods have been developed to produce copper oxide nanowires. Cu_2O can be formed by thermal oxidation of copper above 300°C.[58,59,60] Precursor methods are also utilized, such as a complex-precursor surfactant-assisted route and a reduction route with polyethylene glycol as the surfactant.[61,62] Electrochemical conditions that use platinum as the electrode can produce Cu_2O nanowires, if copper is present in the solution.[63,64]

Fe_3O_4 is a magnetic material with a spinel structure. Iron oxide nanowires can be important for use in magnetic recording material, sensors, pigments, and electronic devices. Many hydrothermal methods to produce Fe_3O_4 nanostructures have been developed, including a microwave hydrothermal process.[65,66,67,68,69] Iron oxide powder was produced through a sonochemical method carried out in an argon atmosphere.[70] Wang *et. al.*[71] synthesized magnetic Fe_3O_4 powders through an arc-electrodeposition method that used iron filaments as the electrodes. A flame synthesis method was utilized by Merchan-Merchan to produce Fe_3O_4 nanorods through a vapor-liquid-solid method that were 10 – 100 nm in diameter. They were introduced into the flame at temperatures ranging from 1330 – 1500 K. The growth mechanism utilizes oxidative removal of iron

from the bottom of the probe and transport with the gaseous species to the top of the probe (material transport/condensation mechanism).[72] In this work, Cu_2O and Fe_3O_4 nanowires are produced through a robust flame synthesis method.

7.2 Experiment

The counterflow diffusion flame (CDF) setup consists of two converging nozzles with a 19 mm diameter and 15 mm separation distance, which can be seen in Figure 7.2(a). The top burner releases air, and the bottom burner issues diluted methane and hydrogen. The methane flame issues fuel composed of 50% nitrogen and 50% methane, while the hydrogen flame issues fuel composed of 63.5% nitrogen and 36.5% hydrogen. The burners have an inert co-flow, in this case nitrogen, to extinguish any outer flame, minimize shear instabilities, and eliminate oxidizer entrainment.

The CDF allows the chemical species to be tailored for given temperature sutiable for gas-phase nanowire synthesis. The flame structure is readily specified using computational simulations. The temperature profiles of the methane and hydrogen flames are purposely matched to compare chemical species. Figure 7.1 shows graphs of the temperature and species concentrations of the two flame structures obtained by computational simulations using GRI-Mech 1.2.[4] The gas phase temperatures and species concentrations are confirmed using spontaneous Raman spectroscopy (SRS), as shown in the Figure 7.2(b).

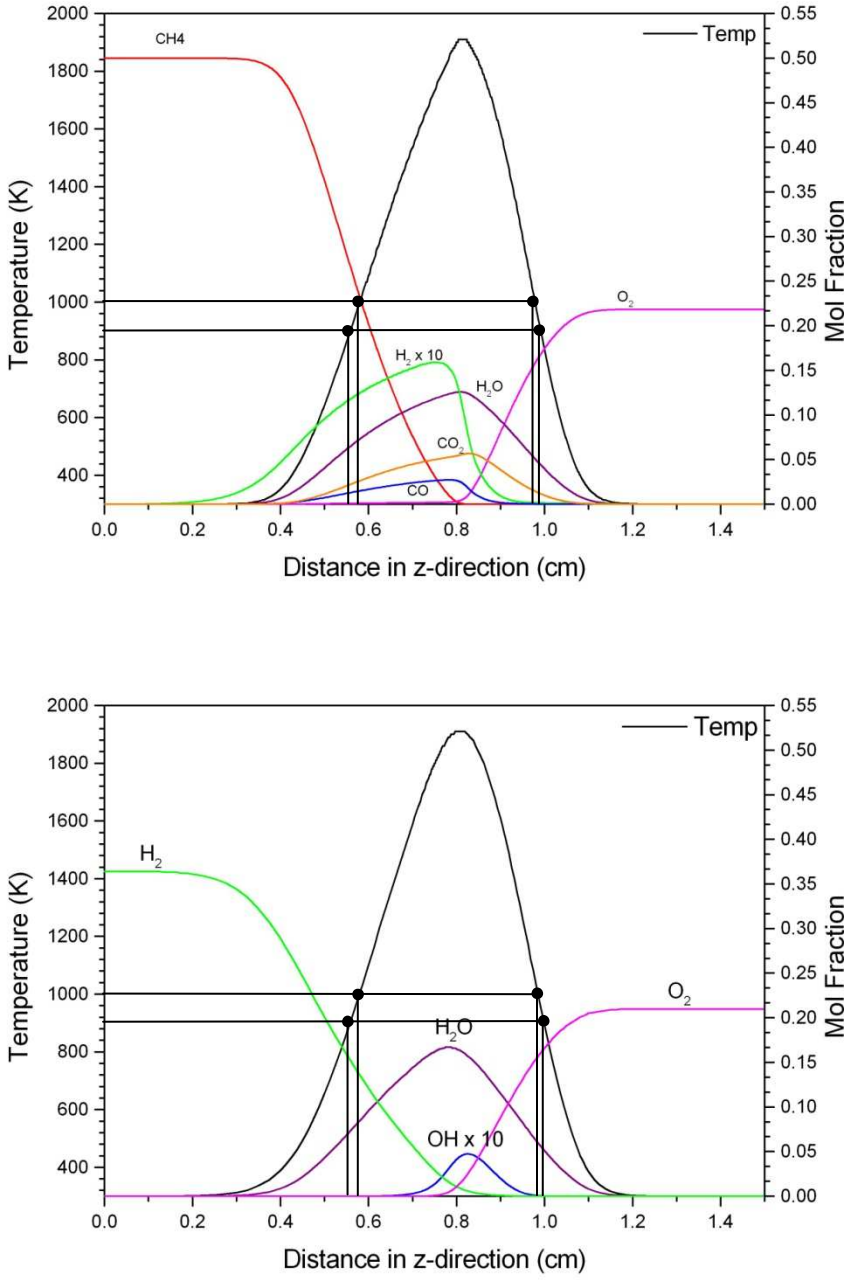

Figure 7.1 Gas phase flame structure of methane and hydrogen flames.

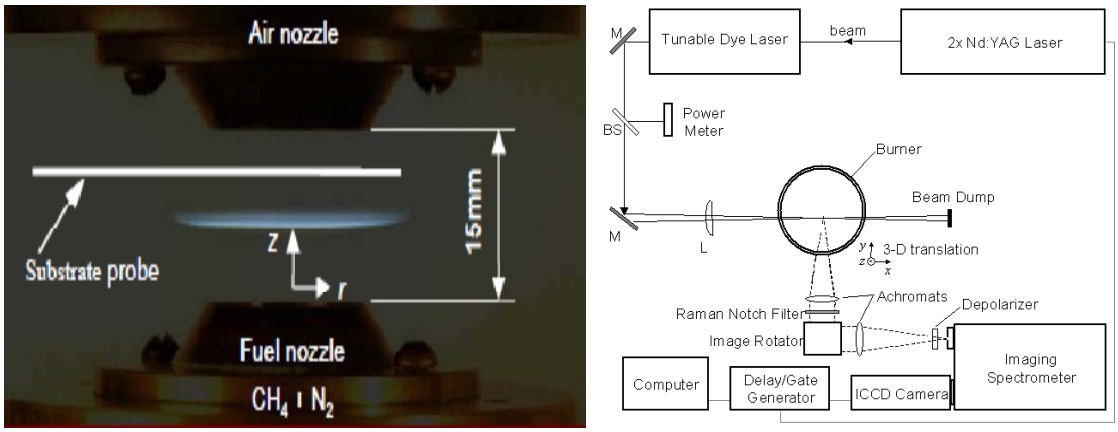

Figure 7.2 (a) Counterflow diffusion flame with probed positions marked. (b) SRS diagnostic setup.

Ultrasonically-cleaned copper and iron substrates are inserted into the CDF at positions on the air and fuel sides of the flame in ambient conditions where the temperatures are ~900K and ~1000K, respectively, for 10 minutes. The morphologies of as-grown nanostructures are examined using field emission scanning electron microscopy (FESEM, LEO Zeiss Gemini 982). Structural features of the nanomaterials are investigated using high resolution transmission electron microscopy (HRTEM, TOPCON 002B), along with selected area electron diffraction (SAED).

7.3 Results

7.3.1 Air Side

Cu_2O nanowires are grown only on the air side of the flames with the densest yield in the methane flame, giving insight into growth mechanisms and conditions that are favorable for nanowires growth. Figure 7.3(a) and (b) show a dense yield of copper oxide nanowires grown at ~900 K in the methane flame. The nanowires are approximately 150 nm in diameter and a few microns in length. On the air side of the hydrogen flame, very

few nanowires grow on the copper substrate, which can be seen in Figure 7.4(a) and (b). These nanowires are about 200 nm in diameter and a few microns in length.

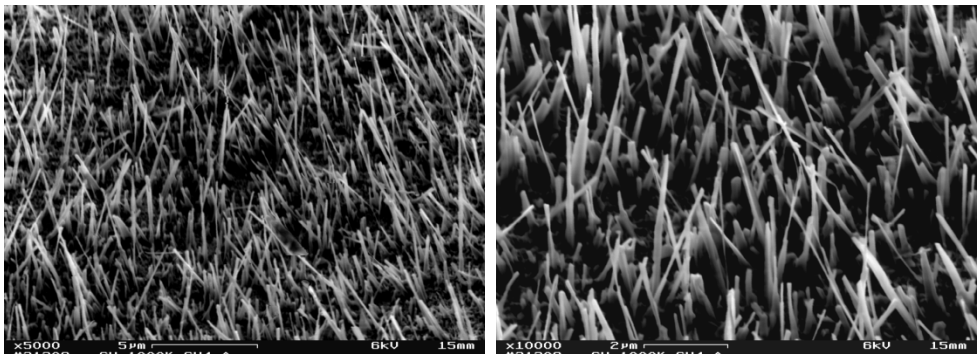

Figure 7.3 (a) Low magnification copper oxide nanowires grown in a CH_4 flame (z=+0.97cm) (b) Magnified FESEM image of nanowires grown in CH_4

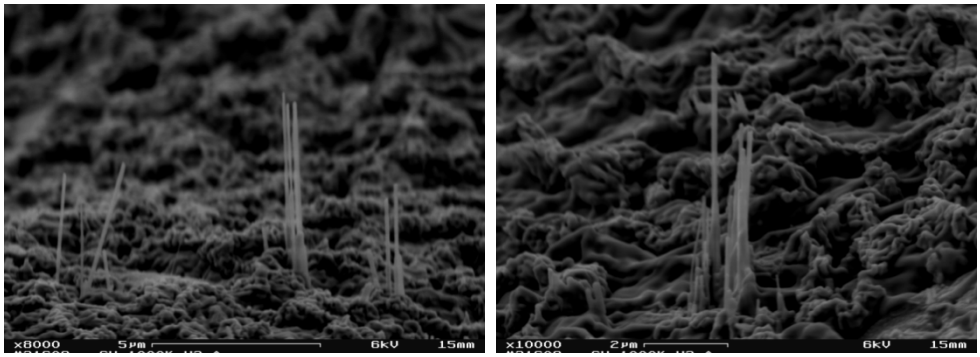

Figure 7.4 (a) Low magnification showing yield of copper oxide from H_2 flame (z=+0.97cm) (b) Typical image of copper oxide grown in the H_2 flame

The concentrations of the gas phase species at the probed location are given in Table 7.1, for the air side of the methane and hydrogen flames. In the methane flame, O_2, H_2O, and CO_2 are present in varying amounts. There is seven times more oxygen gas than water vapor, and ten times more oxygen than carbon dioxide in the methane flame. The hydrogen flame does not have any carbon containing species, but there is six times more oxygen than water vapor. Therefore, the oxygen reaction may be the most dominant in forming the nanowires. The Gibbs free energies[24] are also negative for the reactions shown in Eqns. 7.1 and 7.2. The nanostructure yield is much greater when carbon

dioxide is present in the flame. The reactions for gaseous copper and water vapor and carbon dioxide are negative, but the reactions with solid copper are positive meaning these reactions are not spontaneous. It seems that the vapor-solid growth route is the most probable, with chemical species in the flame adsorbing onto the copper substrate to form nanowires.

$$4Cu^{(s)} + O_2^{(g)} \rightarrow 2Cu_2O^{(s)} \qquad \Delta G_{800K} = -220.2 \qquad (7.1)$$

$$4Cu^{(g)} + O_2^{(g)} \rightarrow 2Cu_2O^{(s)} \qquad \Delta G_{800K} = -1149.6 \qquad (7.2)$$

$$2Cu^{(s)} + H_2O^{(g)} \rightarrow Cu_2O^{(s)} + H_2^{(g)} \qquad \Delta G_{800K} = +93.5 \qquad (7.3)$$

$$2Cu^{(g)} + H_2O^{(g)} \rightarrow Cu_2O^{(s)} + H_2^{(g)} \qquad \Delta G_{800K} = -371.2 \qquad (7.4)$$

$$2Cu^{(s)} + CO_2^{(g)} \rightarrow Cu_2O^{(s)} + CO^{(g)} \qquad \Delta G_{800K} = +103.0 \qquad (7.5)$$

$$2Cu^{(g)} + CO_2^{(g)} \rightarrow Cu_2O^{(s)} + CO^{(g)} \qquad \Delta G_{800K} = -361.7 \qquad (7.6)$$

Air Side		
Species	CH_4 (mol/m^3)	H_2 (mol/m^3)
O_2	71.10	72.50
H_2O	10.70	12.50
CO	0.09	0.00
OH	0.01	0.01
CO_2	6.88	0.00

Table 7.1 Concentrations of species in the methane and hydrogen flame on the air side at ~900K at the probed location (z=+0.97).

A dense yield of Fe_3O_4 nanowires are grown on the air side of the methane and hydrogen diffusion flames at ~1000 K. The fuel side results show some oxidation of the iron as well as carbon nanotube growth. Figure 7.5(a) and (b) are images of the iron oxide

nanowires grown on the air side of the methane flame. The wires are about 150 nm in diameter and a few microns in length. Iron oxide nanowires are also grown in the hydrogen flame, as seen in Figure 7.6(a) and (b). They are ~200 nm in diameter and a few microns in length.

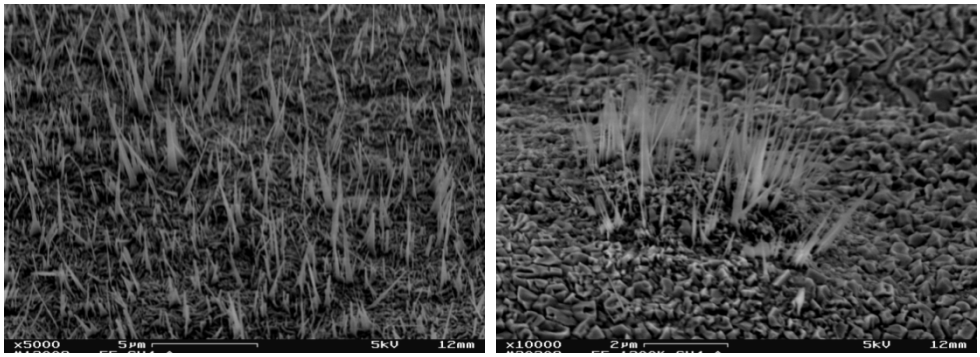

Figure 7.5 (a) Low magnification iron oxide nanowires grown in a CH_4 flame (b) Magnified FESEM image of nanowires grown in CH_4

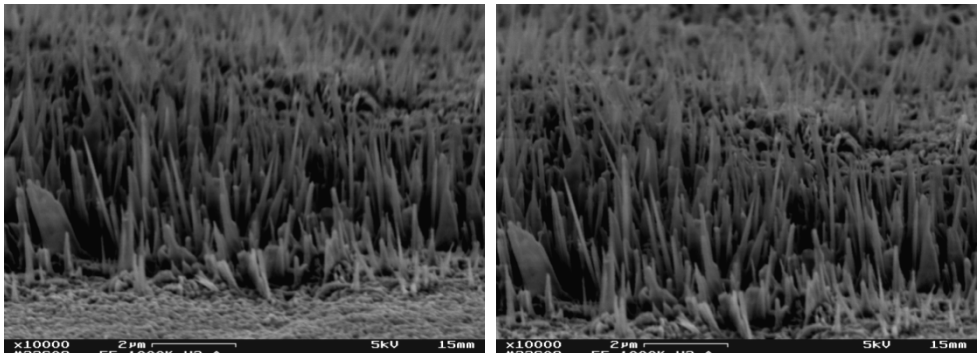

Figure 7.6 (a) Low magnification showing dense yield of iron oxide from H_2 flame (b) Typical image of iron oxide grown in the H_2 flame

Below in Table 7.2, the chemical species concentrations in the methane and hydrogen flames are given. In the methane flame there is almost six times more oxygen than water vapor and almost ten times more oxygen than carbon dioxide. The hydrogen flame does not have any carbon containing species, but there is four times more oxygen than water vapor. All of the Gibbs free energies for the equations 7.7 to 7-12 are negative; therefore, all of the possible reactions can occur spontaneously, but oxygen seems to be the

dominating species in the flame at +0.98 cm. Also, nanowire growth in the methane and hydrogen flames are similar, which makes it appear that carbon dioxide is not a necessary species for Fe_3O_4 nanowire growth. This type of nanowire growth appears to fall into the vapor-solid growth category as well.

$$3Fe^{(s)} + 2O_2{}^{(g)} \rightarrow Fe_3O_4{}^{(s)} \qquad \Delta G_{1000K} = -792.2 \qquad (7.7)$$

$$3Fe^{(g)} + 2O_2{}^{(g)} \rightarrow Fe_3O_4{}^{(s)} \qquad \Delta G_{1000K} = -1586.0 \qquad (7.8)$$

$$3Fe^{(s)} + 4H_2O^{(g)} \rightarrow Fe_3O_4{}^{(s)} + 4H_2{}^{(g)} \qquad \Delta G_{1000K} = -21.3 \qquad (7.9)$$

$$3Fe^{(g)} + 4H_2O^{(g)} \rightarrow Fe_3O_4{}^{(s)} + 4H_2{}^{(g)} \qquad \Delta G_{1000K} = -815.2 \qquad (7.10)$$

$$3Fe^{(s)} + 4CO_2{}^{(g)} \rightarrow Fe_3O_4{}^{(s)} + 4CO^{(g)} \qquad \Delta G_{1000K} = -10.0 \qquad (7.11)$$

$$3Fe^{(g)} + 4CO_2{}^{(g)} \rightarrow Fe_3O_4{}^{(s)} + 4CO^{(g)} \qquad \Delta G_{1000K} = -803.8 \qquad (7.12)$$

Air Side		
Species	CH_4 (mol/m^3)	H_2 (mol/m^3)
O_2	58.80	58.30
H_2O	11.20	13.30
CO	0.10	0.00
OH	0.02	0.02
CO_2	7.84	0.00

Table 7.2 Concentrations of species in the methane and hydrogen flame on the air side at ~1000K at the probed location.

7.3.2 Fuel Side

On the fuel side in the methane and hydrogen flames, no copper-oxide nanowires are grown at 900 K. The surface of the copper substrate appears to be oxidized as shown in Figure 7.7 and Figure 7.8, but no nanowires are formed. Small bright particles are

apparent in Figure 7.7(a) and (b), which are copper oxide. On the substrate in the hydrogen flame, as shown in Figure 7.8(a) and (b), small step-like features are present. It appears that some incipient nucleation sites have formed, but no nanowire growth is seeded from them.

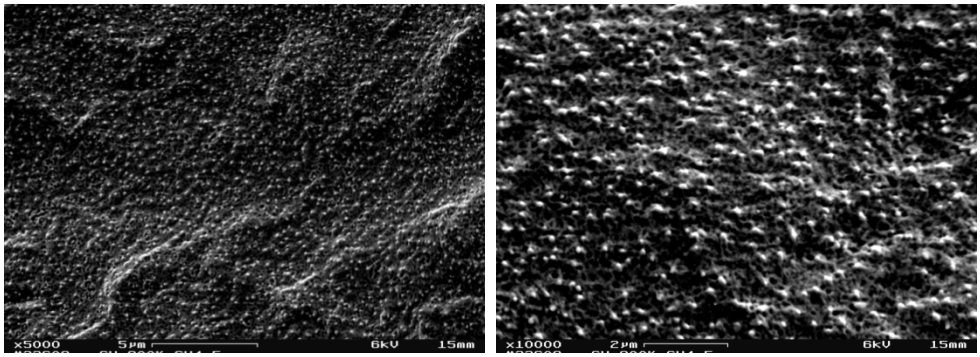

Figure 7.7 (a) Low magnification copper oxide substrate on the fuel side of a CH_4 CDF (b) Magnified image of substrate

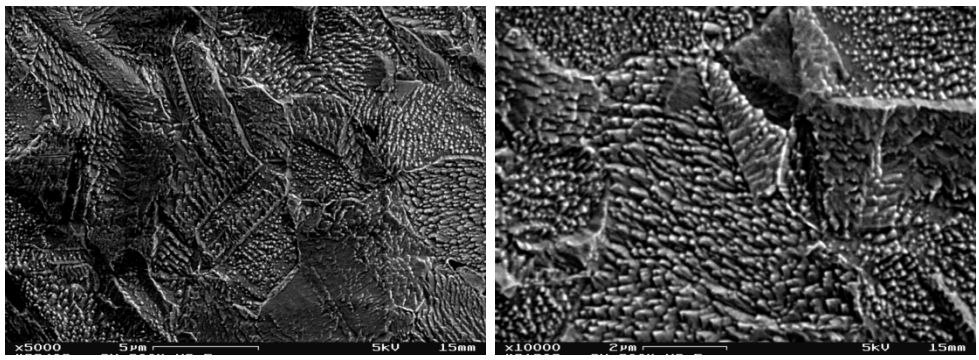

Figure 7.8 (a) Low magnification showing copper oxidation in H_2 flame (b) Typical image of copper oxidation on the fuel side of the H_2 flame

Table 7.3 gives the species concentrations in the methane and hydrogen flames at 900 K. It is apparent that water vapor is the dominant species present. Since no nanowires grow on the substrate, it proves that oxygen gas is the growth mechanism for Cu_2O nanowire formation.

Fuel Side		
Species	CH4 (mol/m^3)	H2 (mol/m^3)
O_2	0.37	0.00
H_2O	15.70	17.90
CO	4.87	0.00
OH	0.00	0.00
CO_2	13.20	0.00

Table 7.3 Species concentrations in methane and hydrogen flame structure on the fuel side at ~900K at the probed location (z=+0.56).

Various structures are found on the fuel side of the iron substrate in the methane flame. Figure 7.9(a) shows catalytic carbon nanotube (CNT) growth. Iron is a catalyst for CNTs; therefore, there is an iron nanoparticle at the end of every CNT. Iron oxide is also grown on the same substrate as well, which can be seen in Figure 7.9(b). They are nanoneedles that are up to 500 nm in length. In the hydrogen flame, iron is oxidized but no nanowires are formed. In Figure 7.10(a) and (b) micron sized structures are shown that are grown in the hydrogen flame on the fuel side.

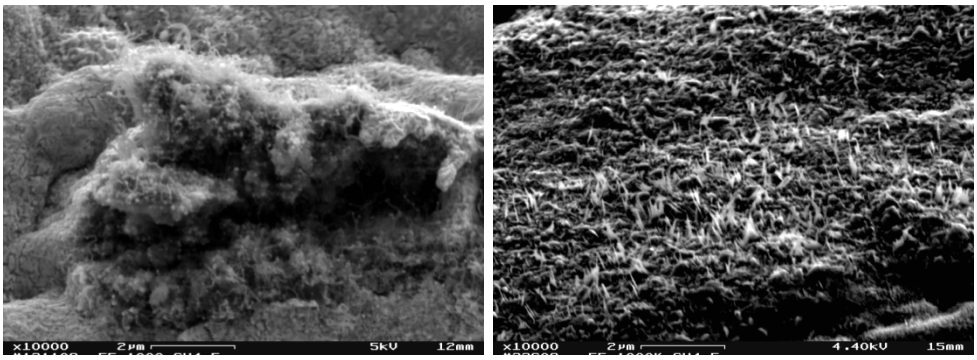

Figure 7.9 (a) Low magnification carbon nanotubes grown on the fuel side of a CH_4 CDF (b) Magnified image of iron oxide nanowires grown in CH_4

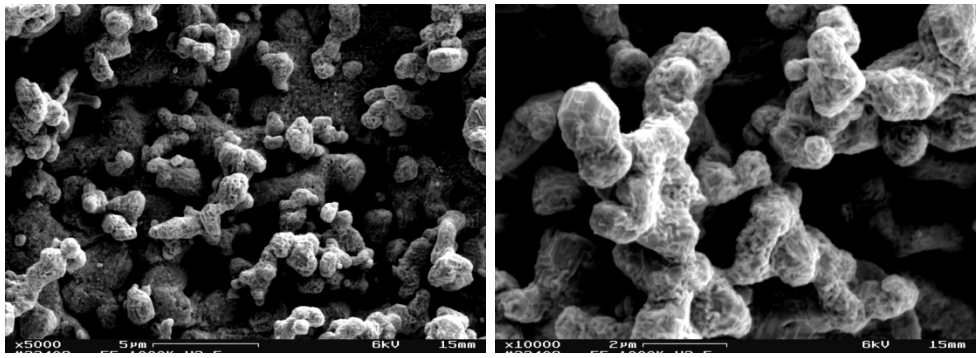

Figure 7.10 (a) Low magnification showing iron oxide from H_2 flame (b) Typical image of iron oxide grown on the fuel side of the H_2 flame

In the methane and hydrogen flame, the species concentrations present are given in Table 7.4. In the methane flame, there is a comparable amount of water vapor and carbon dioxide. It seems as though both species are reacting with the iron because the carbon from CO_2 is reacting to form CNTs, and the oxygen from H_2O is reacting to form iron oxide. Only water vapor is present in the hydrogen flame, and no nanostructrures are formed at 1000 K. There is, however, oxidation of the surface due to the water vapor present in the flame.

Fuel Side		
Species	CH4 (mol/m^3)	H2 (mol/m^3)
O_2	0.39	0.00
H_2O	16.00	18.70
CO	5.06	0.00
OH	0.00	0.00
CO_2	14.00	0.00

Table 7.4 Species concentrations in methane and hydrogen flame structure on the fuel side at ~1000K at the probed location (z=+0.58).

7.4 Conclusion

In summary, a parametric study is performed in order to correlate local growth conditions with morphologies. Cu_2O nanowires are only grown on the air side of the methane and hydrogen flames. Fe_3O_4 nanowires are grown on the air side and fuel side of the methane flame, while nanowires are only found on the air side of the hydrogen flame. Carbon nanotubes are also found on the fuel side of the methane flame. Micron sized structures are grown on the iron substrate on the fuel side of the hydrogen flame.

Chapter 8

Concluding Remarks

8.1 Review of Results

In this work, the growth mechanisms of 1D metal oxide nanostructures are investigated in counterflow diffusion flames. Methane (50% CH_4 and 50% N_2) and hydrogen (36.5% H_2 and 63.5% N_2) flame structures are used to perform parametric studies on the growth mechanisms involved (O_2 vs. H_2O and O_2 vs. CO_2) in the synthesis of $WO_{2.9}$, ZnO, Cu_2O, and Fe_2O_3 nanostructures. In synthesizing MoO_2, a 100% CH_4 flame and 44.0% H_2 / 56.0% N_2 flame are used to in order to attain higher flame temperatures. Flame structures favorable for synthesis (for specific local gas-phase temperatures and relavant species concentrations) are established by using a computational simulation that utilizes chemical kinetics and transport mechanisms. The probe temperatures are examined using an optical pyrometer. Locations within the flame structure with the same temperature but different species concentrations are examined with a base-metal substrate. Then the samples are characterized using SEM and TEM to obtain information on morphology and chemical structure. The morphologies of as-grown nanomaterials can be correlated with local growth conditions.

$WO_{2.9}$ is synthesized using a tungsten substrate in both methane and hydrogen flames at 1720K. Nanowires are found on the air and fuel sides of the probed regions. Any of the routes are possible for tungsten oxide formation in the methane flame, but it seems probable that a hydrothermal route comes into play for the nanowires grown in the

hydrogen flame due to their large diameters. Also, interestingly, no WC_x formation occurs, which may be due to the fact that it has much higher activation energy or that the substrate temperatures are not high enough.

The ZnO nanostructures grown at 1000, 1300, and 1600K contain quite a few different morphologies, such as nanorods, nanosheets, nanoneedles, nanobelts, etc. These different morphologies can be grown by any of the growth routes, such as reactions with water vapor, direct reaction (of zinc droplets or vapor) with oxygen gas, or heterogeneous oxidation by carbon dioxide. Also, none of the Gibbs free energies for the reactions are a limiting factor in O_2, H_2O, or CO_2 growth. A vapor-liquid-solid and vapor-solid growth mechanism may also exist depending on the ZnO formation that occurs.

At 2000K, MoO_2 nanoplates are grown in the methane flame on the air side and fuel side. There is water vapor and carbon dioxide present in similar amounts; therefore, either route may form these nanoplates, with a vapor-solid mechanism causing the formation. On the air side of the hydrogen flame, direct oxidation of the surface by water vapor seems to take place, given the complex structures formed. The fuel side of the hydrogen flame produces large nanoplates, on the micron scale, due to the water vapor route.

Copper oxide (Cu_2O) nanowires are grown primarily on the air side of the methane and hydrogen flames at 900K. On the fuel side, some oxidation of the substrate is seen due to the water vapor present, but no nanowires are formed. This leads to the conclusion that oxygen is the only possible growth mechanism for Cu_2O nanowire growth.

At 1000K Fe_3O_4 nanowires are grown on the air side of the methane and hydrogen flames. It seems oxygen is the leading factor in the growth of the Fe_3O_4 on the air side. On the fuel side of the methane flame, both CNTs and iron oxide are formed, most likely due to the CO present within the flame. Finally, on the fuel side of the hydrogen flame, some oxidation of the surface occurs due to the water vapor present within the flame.

8.2 Future Work

In the methane flame, carbon, hydrogen, and oxygen are present in various amounts. This means that O_2, H_2O, and CO_2 can react with the metals and form metal oxides. In the hydrogen flame, carbon is not present, and only water and oxygen are present for oxidation. The next step to isolate the CO_2 route would be to examine a CO/air flame. This would require a special enclosed setup to perform the parametric studies. Much greater insight would be gained into the growth mechanisms that form metal oxide nanomaterials.

In this work, W, Zn, Mo, Cu, and Fe substrates are utilized in probing various temperatures and species. Other metal substrates that could potentially form metal-oxides with unique properties could also be investigated, such as Al, Bi, and Mg. This would produce a wide array of metal oxide nanowires for various applications and devices.

References

[1] Turns S.R., An Introduction to Combustion: Concepts and Applications, McGraw Hill (1996).
[2] Kee R.J., Rupley F.M., Meeks E., Miller J.A., CHEMKIN-III: A fortran chemical kinetics package for the analysis of gas-phase chemical and plasma kinetics, Rept. SAND96-8216, Sandia national laboratories (1996).
[3] Kee R.J., Dixon-Lewis G., Warnatz J., Coltrin M.E., Miller J.A., Moffat H.K., A fortran computer code package for the evaluation of gas-phase, multicomponent transport properties, Rept. SAND86-8246B, Sandia national laboratories (1998).
[4] M. Frenklach, H. Wang, C.-L Yu, M. Goldenberg, C. T. Bowman, R. K. Hanson, D. F. Davidson, E. J. Chang, G. P. Smith, D. M. Golden, W. C. Gardiner, and V. Lissianski, http://www.me.berkeley.edu/gri mech/; and Gas Research Institute Topical Report: M. Frenklach, H. Wang, M. Goldenberg, G. P. Smith, D. M. Golden, C. T. Bowman, R. K. Hanson, W. C. Gardiner, and V. Lissianski, GRI-Mech-An Optimized Detailed Chemical Reaction Mechanism for Methane Combustion, Report No. GRI–95/0058, November 1 (1995).
[5] M.A. Mueller, T.J. Kim, R.A. Yetter, and F.L. Dryer, Int. J. Chem. Kinet., 31, 113 (1999).
[6] Y. Q. Zhu, W. Hu, W. K. Hsu, M. Terrones, N. Grobert, J. P. Hare, H. W. Kroto, D. R. M. Walton, and H. Terrones, Chem. Phys. Lett. 309, 327 (1999).
[7] H. Qi, C. Wang, and J. Liu, Adv. Mater. 15, 411 (2003).
[8] K. Hong, W. Yiu, H. Wu, J. Gao, and M. Xie, Nanotechnology 16, 1608 (2005).
[9] Y. B. Li, Y. Bando, D. Golberg, and K. Kurashima, Chem. Phys. Lett. 367, 214 (2003).
[10] M. Gillet, R. Delamare, and E. Gillet, Eur. Phys. J. D 34, 291 (2005).
[11] G. Gu, B. Zheng, W. Q. Han, S. Roth, and J. Liu, Nano Lett. 2 849 (2002).
[12] J. Zhou, Y. Ding, S. Z. Deng, L. Gong, N. S. Xu, and Z. L. Wang, Adv. Mater. 17, 2107 (2005).
[13] Y. Z. Jin, Y. Q. Zhu, R. L. D. Whitby, N. Yao, R. Ma, P. C. P. Watts, H. W. Kroto, and R. M. Walton, J. Phys. Chem. B 108, 15572 (2004).
[14] A. Rothschild, J. Sloan, and R. Tenne. J. Am. Chem. Soc. 122, 5169 (2000).
[15] S. Vaddiraju, H. Chandrasekaran, and M. K. Sunkara, J. Am. Chem. Soc. 125, 10792 (2003).
[16] Y. Li, Y. Bando, and D. Golberg, Adv. Mater. _Weinheim, Ger._ 15, 1294 (2003).
[17] Z. Liu, Y. Bando, and C. Tang, Chem. Phys. Lett. 372, 179 (2003).
[18] J. Liu, Y. Zhao, and Z. Zhang, J. Phys.: Condens. Matter 15, L453 (2003).
[19] K. Liu, D. T. Foord, and L. Scipioni, Nanotechnology 16, 10 (2005).
[20] X.-L. Li, J.-F. Liu, and Y.-D. Li, Inorg. Chem. 42, 921 (2003).
[21] X. W. Lou and H. C. Zeng, Inorg. Chem. 42, 6169 (2003).
[22] H. G. Choi, Y. H. Jung, and D. K. Kim, J. Am. Ceram. Soc. 88, 1684 (2005).
[23] S.-J. Wang, C.-H. Chen, R.-M. Ko, Y.-C. Kuo, C.-H. Wong, K.-M. Uang, T.-M. Chen, and B.-W. Liou, Appl. Phys. Lett. 86, 263103 (2005).
[24] I. Barin, Thermochemical Data of Pure Substances, 2 vols, VCH, Weinheim (1989).
[25] J.M. Giraudon, P. Devassine, J.F. Lamonier, L. Delannoy, L. Leclercq, and G. Leclercq, J. of Solid State Chem., 154, 412 (2000).
[26] S. Shanmugam, D.S. Jacob, and A. Gedanken, J. Phys. Chem. B, 109, 19056 (2005).
[27] G.M. Wang, S.J. Campell, A. Calka, W.A. Kaczmarek, J. of Mat. Sci., 32, 1461 (1997).
[28] L.E. Toth, Transition metal carbides and nitrides, Academic Press, New York, p. 13 (1971).
[29] X. Wang, J. Song, Z.L. Wang, J. Mat. Chem., 17, 711 (2007).
[30] C.X. Xu, X.W. Sun, Z.L. Dong, G.P. Zhu, Y.P. Cui, Appl. Phys. Lett. 88, 093101 (2006).
[31] Z.L. Wang, , J. Phys.: Condens. Matter 16, R829 (2004).
[32] Z.L. Wang, Materials Today 7, 26 (2004).
[33] G.C. Yi, C. Wang, W.I. Park, Semicond. Sci. Technol. 20, S22 (2005).
[34] P. X. Gao, C. S. Lao, W. L. Hughes, Z.L. Wang, Chem. Phys. Lett. 408, 174 (2005).
[35] P.X. Gao, Z.L. Wang, Appl. Phys. Lett. 84, 2883 (2004).
[36] J. Y. Lao, J. Y. Huang, D. Z. Wang, and Z. F. Ren, Nano Lett. 3, 235 (2003).
[37] W. Bai, K. Yu, Q. Zhang, F. Xu, D. Peng, and Z. Zhu, Materials Letters 61, 3469 (2007).
[38] Y. Dai, Y. Zhang, and Z. L. Wang, Solid State Communications 126, 629 (2003).

[39] P.A. Hu, Y. Q. Liu, L. Fu, X.B. Wang, D.B. Zhu, Appl. Phys. A, 80, 35 (2005).
[40] A.A. Vostrikov, A.V. Shishkin, N.I. Timoshenko, Tech. Phys. Lett., 33, 30 (2007).
[41] J.M. Osborne, W.J. Rankin, D.J. McCarthy, D.R. Swinbourne, Metal. And Mat. Trans. B, 32B, 37 (2001).
[42] J.Q. Hu, X.L. Ma, Z.Y. Xie, N.B. Wong, C.S. Lee, S.T. Lee, Chem. Phys. Lett., 344, L97 (2001).
[43] F. Wang, L. Cao, A. Pan, R. Liu, X. Wang, X. Zhu, S. Wang, B. Zou, J. Phys. Chem, C, 111, 7655 (2007).
[44] P.X Gao, Z.L Wang, Appl. Phys. Lett. 84, 2883 (2007).
[45] W.J. Moore, Physical Chemistry, 3rd ed. Prentice Hall (1962).
[46] N. A. Dhas, and A. Gedanken, Chem. Mater. 1997, 3144 (1997).
[47] E. Comini, L. Yubao, Y. Brando, G. Sberveglieri, Chem Phys. Lett. 407, 368 (2005).
[48] J. Zhou, N.S. Xu, S.Z. Deng, J. Chen, J.C. She, Chem. Phys. Lett. 382, 443 (2003).
[49] J. Zhou, S.Z. Deng, N.S. Xu, J. Chen, J.C. She, App. Phys. Lett. 83, 2653 (2003).
[50] M. Niederberger, F. Krumeich, H.J. Muhr, M. Muller, and R. Nesper, J. of Mat. Chem. 11, 1941 (2001).
[51] Y.B. Li, Y. Bando, D. Goldberg, and K. Kurashima, App. Phys. Lett. 81, 5048 (2002).
[52] Y. Li, Y. Bando, Chem. Phys. Lett. 364, 484 (2002).
[53] M. Suemitsu, T. Abe, H.J. Na, and H. Yamane, Jap. J. of App. Phys. 44, L449 (2005).
[54] W. Merchan-Merchan, A.V. Saveliev, L.A. Kennedy, Chem. Phys. Lett. 442, 72 (2006).
[55] E. A. Gulbransen, K.F. Andrew, and F.A. Brassart, J. of the Electrochem. Soc. 110, 958 (1963).
[56] N. A. Gokcen, J. of Metals. 1019 (1953).
[57] H. M. Spencer, and J.L. Justice, J. of the Am. Chem. Soc. 1934, 2301 (2002).
[58] L.S. Huang, S.G. Yang, T. Li, B.X. Gu, Y.W. Du, Y.N. Lu, S.Z. Shi, J. of Crystal Growth, 260, 130 (2004).
[59] C.H. Xu, C.H. Woo, S.Q. Shi, Superlattices and Microstructures, 36, 31 (2004).
[60] X. Jiang, T. Herricks, Y, Xia, Nanoletters, 2, 1333 (2002).
[61] W. Wang, G. Wang, X. Wang, Y. Zhan, Y. Liu, C. Zheng, Adv. Mat., 14, 67 (2002).
[62] Y. Xiong, Z. Li, R. Zhang, Y. Xie, J. Yang, C. Wu, J. Phys. Chem. B., 107, 3697 (2003).
[63] E. Ko, J. Choi, K. Okamoto, Y. Tak, J. Lee, ChemPhysChem, 7, 1505 (2006).
[64] D.P. Sing, N.R. Neti, A.S.K. Sinha, O.N. Srivastava, J. Phys. Chem. C, 111, 1638 (2007).
[65] Y.B. Khollam, S.R. Dhage, H.S. Potdar, S.B. Deshpande, P.P. Bakare, S.D. Kulkarni, S.K. Date, Materials Letters, 56, 571 (2002).
[66] S. Lian, E. Wang, L. Gao, Z. Kang, D. Wu, Y. Lan, L. Xu, Solid State Comm., 132, 375 (2004).
[67] J. Wan, Y. Yao, G. Tag, Appl. Phys. A, 89, 529 (2007).
[68] R. Fan, X.H. Chen, Z. Gui, L. Liu, Z.Y. Chen, Mat. Research Bulletin, 36, 497 (2001).
[69] D. Chen, R. Xu, Mat. Research Bulletin, 33, 1015 (1998).
[70] R. Vijayakumar, Y. Koltypin, I. Felner, A. Gedanken, Materials Science and Engineering, A286, 101 (2000).
[71] C.Y. Wang, G.M. Zhu, Z.Y. Chen, Z.G. Lin, Mat. Research Bulletin, 37, 2525 (2002).
[72] W. Merchan-Merchan, A.V. Saveliev, A.M. Taylor, Nanotechnology, 19, 125065 (2008).